MNRAS **000**, 1–17 (2016) Preprint 2 August 2016 Compiled using MNRAS LATEX style file v3.0

A Robust Measurement of the Mass Outflow Rate of the Galactic Outflow from NGC 6090

John Chisholm[1⋆], Christy A. Tremonti[1], Claus Leitherer [2], Yanmei Chen[3]
[1] *Astronomy Department, University of Wisconsin, Madison, 475 N. Charter St., WI 53711, USA*
[2] *Space Telescope Science Institute, 3700 San Martin Drive, Baltimore, MD 21218, USA*
[3] *Department of Astronomy, Nanjing University, Nanjing 210093, China*

arXiv:1605.05769v2 [astro-ph.GA] 1 Aug 2016

2 August 2016

ABSTRACT

To evaluate the impact of stellar feedback, it is critical to estimate the mass outflow rates of galaxies. Past estimates have been plagued by uncertain assumptions about the outflow geometry, metallicity, and ionization fraction. Here we use Hubble Space Telescope ultraviolet spectroscopic observations of the nearby starburst NGC 6090 to demonstrate that many of these quantities can be constrained by the data. We use the Si IV absorption lines to calculate the scaling of velocity (v), covering fraction (C_f), and density with distance from the starburst (r), assuming the Sobolev optical depth and a velocity law of the form: $v \propto (1 - R_i/r)^{\beta}$ (where R_i is the inner outflow radius). We find that the velocity (β=0.43) is consistent with an outflow driven by an r^{-2} force with the outflow radially accelerated, while the scaling of the covering fraction ($C_f \propto r^{-0.82}$) suggests that cool clouds in the outflow are in pressure equilibrium with an adiabatically expanding medium. We use the column densities of four weak metal lines and CLOUDY photoionization models to determine the outflow metallicity, the ionization correction, and the initial density of the outflow. Combining these values with the profile fitting, we find $R_i = 63$ pc, with most of the mass within 300 pc of the starburst. Finally, we find that the maximum mass outflow rate is 2.3 $M_\odot$ yr^{-1} and the mass loading factor (outflow divided by the star formation rate) is 0.09, a factor of 10 lower than the value calculated using common assumptions for the geometry, metallicity and ionization structure of the outflow.

Key words: ISM: jets and outflows, galaxies: evolution, galaxies: formation, ultraviolet: ISM

1 INTRODUCTION

Strangely, most of the gas within a galaxy is not near stars (Songaila 1997; Adelberger et al. 2003; Tumlinson et al. 2011; Werk et al. 2014; Peeples et al. 2014; Wakker et al. 2015). The circum-galactic medium extends to radii greater than 150 kpc, is metal rich, and spans a range of temperatures (Songaila 1997; Werk et al. 2014; Peeples et al. 2014). Further, this reservoir of gas is massive, containing up to three times more mass than gas within discs (Werk et al. 2014). Even though the gas extends more than 150 kpc from the stellar disc, the metal enrichment implies that the gas originated within the stellar disc. What could loft so much mass out of discs?

High-mass stars inject energy and momentum into the ISM through high energy photons, cosmic rays, and supernovae, together commonly called stellar feedback (Weaver et al. 1977; McKee & Ostriker 1977; Chevalier & Clegg 1985; Heckman et al. 1990; Murray et al. 2005; Thompson et al. 2005; Everett et al. 2008; Socrates et al. 2008; Hopkins et al. 2012, 2014a; Kim & Ostriker 2015; Kimm et al. 2015; Bustard et al. 2016). If the stellar feedback is highly concentrated, then the combined energy and momentum drives gas out of star forming regions into a galactic outflow (Heckman et al. 1990, 2000; Veilleux et al. 2005; Erb 2015). Galactic outflows may enrich the large reservoir of cirum-galactic gas, while also removing metals from low-mass galaxies to create the mass-metallicity relation (Tremonti et al. 2004; Finlator & Davé 2008; Peeples & Shankar 2011; Andrews & Martini 2013; Zahid et al. 2014; Creasey et al. 2015; Christensen et al. 2015). However, accurate mass outflow rates are required to constrain these relations.

Observations of galactic outflows are challenging. First, galactic outflows are multi-phase, with emission from hot

⋆ Contact email: chisholm@astro.wisc.edu

© 2016 The Authors

X-ray emitting plasma (Griffiths et al. 2000; Strickland & Stevens 2000; Strickland & Heckman 2009), to ionized hydrogen (Lynds & Sandage 1963; Bland & Tully 1988; Shopbell & Bland-Hawthorn 1998; Westmoquette et al. 2009; Newman et al. 2012; Arribas et al. 2014), and even cold molecular gas (Weiß et al. 1999; Matsushita et al. 2000; Leroy et al. 2015). Second, outflows are diffuse, and probing outflows with emission lines is challenging and limited to only the local universe. Recent studies use optical (Heckman et al. 2000; Martin 2005; Rupke et al. 2005b; Chen et al. 2010), near UV (Weiner et al. 2009; Martin & Bouché 2009; Steidel et al. 2010; Diamond-Stanic et al. 2012; Kornei et al. 2012; Erb et al. 2012; Rubin et al. 2014) and far UV absorption lines (Pettini et al. 2000, 2002; Shapley et al. 2003; Grimes et al. 2009; Leitherer et al. 2013; Chisholm et al. 2015; Heckman et al. 2015; Wood et al. 2015; Chisholm et al. 2016) to study the diffuse gas within outflows. While these studies have hinted at the role outflows play in removing gas from the discs of galaxies, the mass outflow rate calculations are plagued by uncertain assumptions.

To calculate the mass outflow rate from absorption lines, an observed column density and velocity are converted into a total mass outflow rate. The first step converts the observed ion density to a total Hydrogen density through an assumed metallicity and ionization correction (Rupke et al. 2005b; Heckman et al. 2015). The Hydrogen column density is then converted into a total Hydrogen mass through an assumed geometry, typically a thin shell. These studies make four key assumptions: (1) that the absorption lines are optically thin (2) that the measured ion is the dominant ionization state, and there is no ionization correction (3) that the metallicity of the outflow is consistent with the ISM of the galaxy and (4) that the outflow is a spherical shell with a radius of 5 kpc (Rupke et al. 2005b; Weiner et al. 2009).

Recent observations question these assumptions. Ionization modelling from Chisholm et al. (2016) find that galactic outflows are photoionized, with the dominant ionization state, Si III, at an ionization potential near 25 eV, with only 1-5% of the gas in the neutral phase. For neutral ions like Na I, neglecting the ionization correction can underestimate the total Hydrogen column density by a factor of 4 (Murray et al. 2007; Chisholm et al. 2016). Additionally, these photoionization models predict that the outflows are metal rich, and the assumption that the outflow has the metallicity of the ISM underpredicts the total Hydrogen density.

These large ionization fractions also imply that the outflow is relatively close to the ionizing source. Stars generate outflows at distances of super-star clusters, 20-40 pc (McKee & Ostriker 1977; Weaver et al. 1977; Chevalier & Clegg 1985), but metal-enriched gas is also observed out to 10 kpc from the starburst (Veilleux et al. 2003; Strickland et al. 2004; Rubin et al. 2011; Tumlinson et al. 2011). Even though the outflow extends over this enormous distance, studies typically calculate the mass outflow rates as if the entire mass is in a thin shell with a radius of 5 kpc (Rupke et al. 2005a).

Here, we present a new analysis of the mass outflow rate of the nearby galaxy NGC 6090 using *Hubble Space Telescope* ultraviolet spectroscopy. We calculate the mass outflow rate by first measuring the distance, metallicity, and ionization fraction of the outflow. In § 2 we describe the data reduction, stellar continuum fitting, and measurement of the outflow properties. We then fit for how the optical depth and covering fraction scales with velocity, using a Sobelev optical depth, a β velocity law, and a power-law density scaling (§ 3). We apply the ionization models of Chisholm et al. (2016) to the outflow of NGC 6090 to determine the metallcity (1.61 $Z_\odot$), total Hydrogen density (18.73 cm^{-3}), and the ionization fractions of the outflow (§ 4). In § 5.1 we consider the implications of the ionization models and the metal enriched outflows, and then calculate the initial radius of the outflow (63 pc). Using these derived quantities, we examine the covering fraction (§ 5.2), velocity (§ 5.3), and density (§ 5.4) laws with radius. Since these relationships vary with velocity, we find that the mass outflow rate of the galaxy also varies with velocity, with a maximum mass outflow rate of 2.3 $M_\odot$ yr^{-1}. This mass outflow rate is 10 times smaller than it would be if we used previous assumptions, and only 9% of the star formation rate of the galaxy.

In this paper we use $\Omega_M = .28$, $\Omega_\Lambda = .72$ and $H_0 = 70$ km s^{-1} Mpc^{-1} (Jarosik et al. 2011).

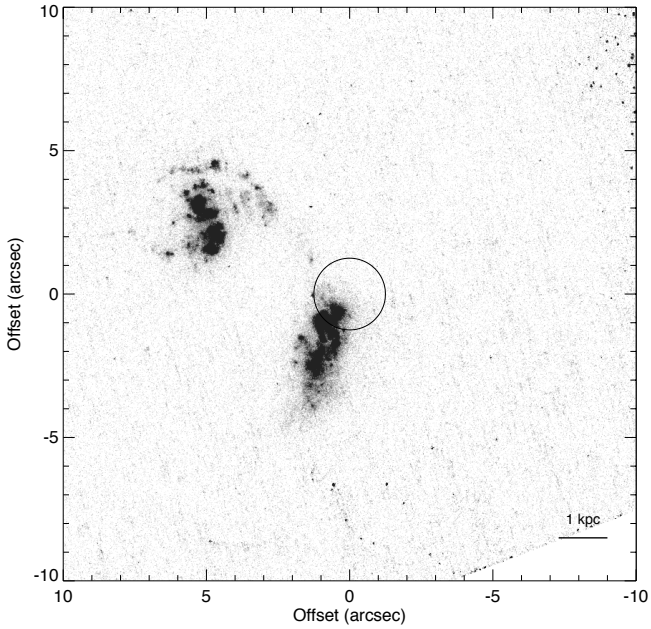

Figure 1. Restframe UV image of NGC 6090 taken with the HST/ACS HRC camera and the F220W filter (restframe central wavelength of 2312 Å). Two distinct nuclei are seen, along with a faint tidal-tail of UV emission in the bridge between the two nuclei. The approximate COS aperture location and size (2.″5 in diameter) are denoted by the black circle. A 1 kpc scale bar is given in the lower right corner, and 1.″0 is equal to 587 pc, at the distance of NGC 6090.

2 DATA

NGC 6090 is a massive star forming galaxy at a distance of 128 Mpc (see Table 1), with no indication of AGN contamination from the optical emission lines (see Table 1) and the *WISE* colors. The galaxy is metal rich, with a log(O/H)+12 of 8.77 (Storchi-Bergmann et al. 1994). The galaxy is in the intermediate stages of a massive merger, as two distinct nu-

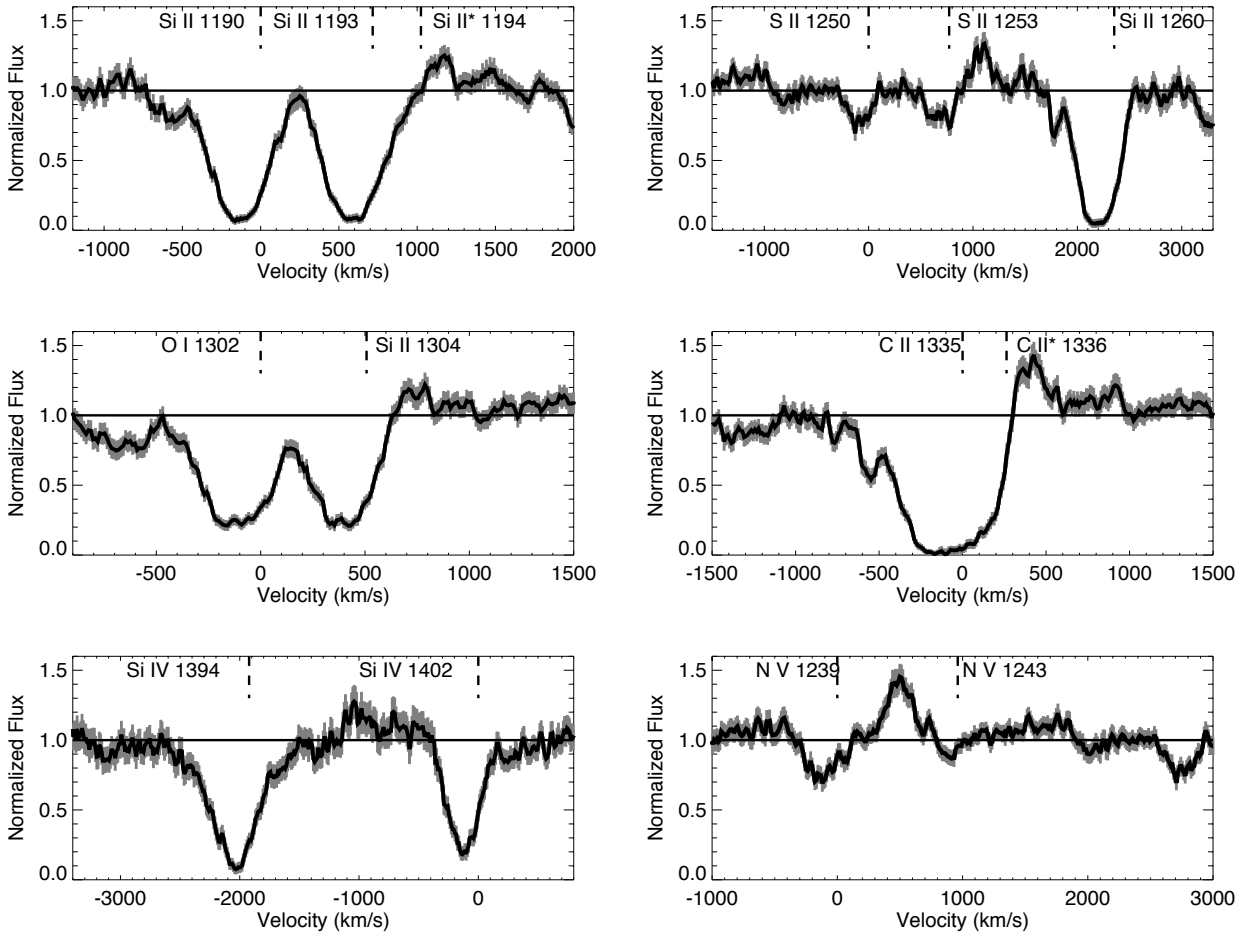

Figure 2. Stellar continuum normalized absorption profiles as the thick black line. The gray envelope around the black line represents the 1σ error on the flux measurement. Multiple transitions are plotted in each panel, and the velocity axis is only for the transition near zero velocity. The zero velocities of all of the transitions are marked and labelled by vertical dashed lines in the upper portions of the plots.

clei and large extend tidal tails are seen in the UV (Figure 1) and optical images (Östlin et al. 2009).

The Cosmic Origins Spectrograph (COS; Green et al. 2012) on the *Hubble Space Telescope* observed NGC 6090 during Cycle 18 (Project ID: 12173; Leitherer et al. 2013). The full data reductions are given in Chisholm et al. (2015), and here we summarize the steps taken to measure the optical depths, covering fractions, and column densities of the outflow. First, we describe the data reductions (§ 2.1) and the stellar continuum fitting (§ 2.2). We then explore the effects of the Si II fine structure and resonance emission lines (§ 2.3). Finally, the optical depths, covering fractions, and column densities are measured in § 2.4.

2.1 Data Reduction

Leitherer et al. (2013) observed NGC 6090 with the G130M grating for a total integration time of 8096 s. We downloaded the spectra from MAST and processed the data through the CalCOS pipeline, version 2.20.1. The individual exposures were aligned and co-added following the methods outlined in Wakker et al. (2015). The spectrum was deredshifted using the redshift from de Vaucouleurs et al. (1991). The flux was normalized to the median flux in a line free region between 1310-1320 Å in the restframe, the wavelength array was then binned by 5 pixels (10 km s^{-1}at 1400Å), and smoothed by 3 pixels. The set-up of the G130M grating affords continuous wavelength coverage between 1125-1425 Å, in the restframe. Our fully processed data have a median signal-to-noise ratio of 12 per pixel after rebinning.

2.2 Stellar Continuum Fitting

Metal absorption in stellar atmospheres contaminates the ISM absorption profiles. To remove the stellar contribution, we fit the observed spectrum with a linear combination of STARBURST99 simple stellar populations models (Leitherer et al. 1999, 2010). To match the resolution of the

Row Number	Property	Value
(1)	$\log_{10}(M_*/M_\odot)$	10.7
(2)	SFR_{tot}	25.15 $M_\odot$ yr^{-1}
(3)	SFR_{COS}	5.55 $M_\odot$ yr^{-1}
(4)	Inclination	29°
(5)	z	0.0293
(6)	D	128 Mpc
(7)	log(O/H) + 12	8.77 dex (1.2 $Z_\odot$)
(8)	log(SII/Hα)	-0.69
(9)	log(OIII/Hβ)	-0.34
(10)	E(B-V)	0.316
(11)	Z_s	1.0 $Z_\odot$
(12)	< Age >	4.478 Myr
(13)	Resolution	48 km s^{-1}

Table 1. Host galaxy properties of NGC 6090. The stellar mass (row 1), total star formation rate (SFR_{tot}; row 2), extinction (row 10), stellar metallicity (row 11), and average stellar age (row 12) are calculated in Chisholm et al. (2016), while the SFR within the COS aperture (SFR_{COS}; row 3), the inclination (row 4), and the spectral resolution (column 11) are from Chisholm et al. (2015). The redshift (row 5) and distance (row 6) are taken from de Vaucouleurs et al. (1991), while the gas phase metallicity (row 7) is from Storchi-Bergmann et al. (1994). The log(SII/Hα) and log(OIII/Hβ) values are from the JHU-MPA SDSS DR7 catalog (Abazajian et al. 2009; Brinchmann et al. 2004), and show that the galaxy is within the star forming locus defined by Kewley et al. (2006).

observations, and to avoid stellar libraries with Milky Way contamination, we use the fully theoretical Geneva models, with high-mass loss (Meynet et al. 1994), computed using the WM-basic method (Leitherer et al. 1999, 2010).

A linear combination of different age stellar populations is required to simultaneously recover the Si III photospheric lines near 1295 Å (signatures of B stars) and the Si IV and N V P-Cygni profiles (signatures of O stars). Since O and B stars dominate the FUV stellar continuum, we include STARBURST99 models of ten ages between 1-20 Myr, and use MPFIT (Markwardt 2009) to determine the linear combination of these ten models. Five ages contribute to the stellar continuum of NGC 6090 (1, 3, 4, 5, 20 Myr), but the 4 and 5 Myr models account for 84% of the FUV light, for a weighted stellar age of 4.48 Myr (see Table 1). The stellar continuum fit is shown in the upper panel of Figure 2 in Chisholm et al. (2016). This figure shows that the STARBURST99 models nicely reproduce the stellar P-Cygni features, and provide a continuum level for the spectrum.

Both the stellar age and metallicity determine the number of ionizing photons emitted by high-mass stars (Leitherer et al. 1999). Accordingly, we fit for both the metallicity and stellar age. STARBURST99 models have five stellar continuum metallicities – 0.05, 0.2, 0.4, 1.0, 2.0 $Z_\odot$ – and we determine that the stellar metallicity of NGC 6090 is solar using a χ^2 test (Table 1). During the fitting, we include continuum reddening using a Calzetti extinction law (Calzetti et al. 2000), and find that the stellar continuum is extincted by E(B-V) = 0.316 mags, after accounting for foreground Milky Way extinction (Schlegel et al. 1998). We cross-correlate the fitted stellar continuum with the observed spectrum to establish the zero-velocity of the stellar continuum. Finally, we remove the stellar continuum by dividing the observed spectrum by the STARBURST99 model.

Strong Milky Way absorption and geocoronal emission lines are blueshifted from the metal lines of NGC 6090. However, the Milky Way lines are masked during the stellar population fitting to avoid contaminating the fit. Since the galaxy non-uniformly fills the COS aperture (see Figure 1), the spectral resolution is degraded. The COS spectral resolution varies from 20 km s^{-1} for a point source to 200 km s^{-1} for a uniformly filled aperture (France et al. 2009). We fit the line width of the Milky Way absorption features, and find that the effective spectral resolution of the spectrum is 48 km s^{-1}.

Figure 2 gives the metal absorption profiles from the fully reduced, stellar continuum normalized spectra. There is a weak C I 1277Å Milky Way absorption line near the N V 1243 Å transition and the stellar continuum is slightly underestimated. While we fit, and remove this weak C I feature, imperfect subtraction creates residual emission, contaminating the continuum near the weaker N V 1243 Å line. Therefore, we do not draw conclusions from the N V profiles.

2.3 Fine Structure Emission Lines

Before we measure the outflow properties from the metal absorption lines, we must understand how resonance emission lines affect the absorption profiles (Prochaska et al. 2011; Rubin et al. 2011; Scarlata & Panagia 2015; Zhu et al. 2015). Continuum photons excite ground state electrons, and the electron then transitions into a lower energy state by emitting a photon with an energy of the difference between the two states. If the electron transitions back to the ground state through the same path as it was excited, it is called resonance emission. Resonant photons have the same rest-frame wavelength as the absorption and, depending on the geometry of the outflow, the resonance emission can overlap in velocity space with the absorption. This effectively reduces the measured absorption profile.

The amount, and the velocity, of the infilling can be estimated if fine structure splits the ground state. The electron's angular momentum splits the ground state into multiple levels, allowing the electron to transition through either resonance or fine structure emission (fine structure emission is normally denoted by a *, i.e. as Si II*). The probability of transitioning by a specific path is given as $P_i = A_i/\Sigma A_i$, where A_i is the Einstein A coefficient corresponding to level i, and the summation is over all possible levels. Therefore, we use the observed fine structure emission to estimate an upper limit on the in-filling of resonance profile.

There are four Si II* lines in the observed wavelength regime at 1194, 1197, 1265, and 1309Å, however the 1265 line is blended with the O I geocoronal emission line. The 1194Å line has the largest probability of fine structure emission (84% of the 1190Å absorption is re-emitted as 1194Å Si II*), therefore this line predicts the maximum amount of resonance emission. The 1194 Si II* line is the strongest of the four Si II* lines in the bandpass, but the equivalent width is only −0.15 Å, a small fraction of the 1.74 Å Si II 1190 Å equivalent width. Further, the line is redshifted by +132 km s^{-1}, with emission only extending to -80 km s^{-1}.

Below, we chiefly use the Si IV doublet, which does not have fine structure emission lines in the wavelength regime. The Si II and Si IV profiles have similar velocity profiles (Chisholm et al. 2016), allowing for the Si II* to be used as a

(1) Line	(2) Equivalent Width (Å)	(3) Velocity Range (km s^{-1})	(4) log(N) (log(cm^{-2}))
O I 1302	1.36 ± 0.02	(-470, 150)	15.46 ± 0.03
Si II 1190	1.74 ± 0.03	(-730, 250)	14.99 ± 0.03
Si II 1193	1.59 ± 0.02	(-465, 300)	14.64 ± 0.02
Si II 1260	1.92 ± 0.02	(-635, 205)	14.40 ± 0.02
Si II 1304	1.12 ± 0.02	(-360, 190)	15.12 ± 0.03
S II 1250	0.24 ± 0.02	(-300, 110)	15.50 ± 0.17
S II 1253	0.23 ± 0.02	(-300, 110)	15.19 ± 0.18
C II 1335	2.99 ± 0.02	(-810, 300)	15.59 ± 0.01
Si III 1206	2.58 ± 0.03	(-780, 430)	14.44 ± 0.02
Si IV 1394	2.16 ± 0.04	(-680, 430)	14.64 ± 0.04
Si IV 1402	1.18 ± 0.03	(-400, 160)	14.63 ± 0.04
N V 1239	0.31 ± 0.02	(-340, 130)	14.22 ± 0.16
N V 1243	0.07 ± 0.01	(-170, 60)	13.83 ± 0.33

Table 2. Table of the absorption line properties for the 13 observed metal lines. The ions and wavelengths are given in column 1. The measured equivalent width, the velocity range integrated over, and the column density of each transition are given in columns 2, 3, and 4, respectively. Many of the strong lines suffer from saturation effects, therefore we only use column densities from the Si IV 1402Å, O I 1302Å, Si II 1304Å, and S II 1250Å lines.

proxy for the Si IV emission. To avoid possible contributions from resonance emission, we exclude velocities greater than -80 km s^{-1} when fitting the profiles in § 3.

2.4 Equivalent Width, Optical Depth, Covering Fraction, and Column Density

Once we have reduced the data, removed the stellar continuum, and explored the impact of the resonance emission features, we measure the properties of the outflow. Here, we describe the outflow with four parameters: equivalent width (W), optical depth (τ), covering fraction (C$_f$), and column density (N).

W is measured by integrating $1 - F_o$ (the observed continuum normalized flux) over the velocity ranges given in column three of Table 2. As discussed in Chisholm et al. (2016), the maximum velocity of each transition strongly depends on the strength (the W) of the transition, not the ionization state of the transition. The W errors are computed by bootstrapping the observed flux with the flux error array 1000 times, and the standard deviation is calculated from the resultant W distributions. The equivalent width ratios of doublets (and triplets) can be used to diagnose the saturation of the transitions. With an observed doublet ratio of 1.83 (and an expected ratio of 2), the Si IV 1402Å and 1392Å lines are the only doublet that does not suffer from severe saturation effects. We also use the column densities of the weak S II 1250Å, Si II 1304Å, and O I 1302Å lines during the ionization modelling (see § 4).

C$_f$ is the fraction of the continuum source covered by the foreground absorbing gas (see Rupke et al. (2005a) for a thorough description of the interpretation of C$_f$). At low τ, C$_f$ and τ are degenerate because both impact the depth of the absorption profile. However, this degeneracy can be broken by solving the radiative transfer equation for the C$_f$ and optical depths of the lines (Hamann et al. 1997). Here, we use the Si IV doublet because it does not suffer from strong saturation effects. The covering fraction is calculated in each pixel to give a velocity (v) resolved C$_f$ profile as (Hamann et al. 1997)

$$C_f(\mathrm{v}) = \frac{\mathrm{F_W(v)}^2 - 2\mathrm{F_W(v)} + 1}{\mathrm{F_S(v)} - 2\mathrm{F_W(v)} + 1} \quad (1)$$

where F$_W$ is the continuum normalized flux of the weaker doublet line (Si IV 1402Å), and F$_S$ is the continuum normalized flux of the stronger doublet line (Si IV 1394). In this equation we use the fact that the Si IV 1402 line has half the oscillator strength of the 1392 line. We set unphysical C$_f$ values that are less than zero to zero. We also calculate the velocity resolved τ as

$$\tau(\mathrm{v}) = \ln\left(\frac{C_f(\mathrm{v})}{C_f(\mathrm{v}) + F_\mathrm{W}(\mathrm{v}) - 1}\right) \quad (2)$$

We bootstrap the errors of C$_f$ and τ, similar to the W errors above.

Finally, we calculate the integrated column density of each transition using the apparent optical depth method (Savage & Sembach 1991). Since some of the weak lines are singlets, we cannot use Equation 1 to calculate the column density, rather we have to assume that the lines are fully covered. Below, we find that this assumption is fair for the line centers, which have most of the column density. The integrated column density is calculated as

$$\mathrm{N} = \frac{3.77 \times 10^{14}\ \mathrm{cm}^{-2}}{\lambda[\text{Å}] f} \int \ln\frac{1}{F_\mathrm{o}(\mathrm{v})}\mathrm{dv} \quad (3)$$

where f is the oscillator strength (Chisholm et al. 2016), and the total N is calculated by integrating over the velocity interval given in Table 2. With the measured properties of the outflow, we now study how the Si IV 1402Å optical depth and covering fraction evolve with velocity.

3 PROFILE FITTING

In Figure 2 the metal absorption lines are broad ($\sim$ 175 km s^{-1}) and blueshifted by ~ -150 km s^{-1}. Under the Sobolev approximation, these profiles are produced by an expanding medium, that has a steep velocity gradient (dv/dr) but a narrow intrinsic line profile, such that the expanding medium broadens the line profile by absorbing and scattering continuum photons (Sobolev 1960; Lamers & Cassinelli 1999; Prochaska et al. 2011; Scarlata & Panagia 2015). The Sobolev optical depth of the Si IV 1402Å profile is given by

$$\tau\,(\mathrm{v}) = \frac{\pi e^2}{\mathrm{mc}} f\lambda\ \mathrm{n_4}\,(\mathrm{r})\,\frac{\mathrm{dr}}{\mathrm{dv}} \quad (4)$$

where f is the oscillator strength (0.255 for Si IV), λ is the rest wavelength, and n$_4$ is the number density of the Si IV gas at a given radius (r). To simplify the calculation, we introduce normalized quantities by dividing the velocity by the maximum velocity ($w = \mathrm{v}/\mathrm{v}_\infty$, $\mathrm{v}_\infty = -399$ km s^{-1} for Si IV 1402Å) and the radius by the inner radius ($x = \mathrm{r}/\mathrm{R_i}$), which we measure in § 5.1. v$_\infty$ is calculated as the velocity at which the absorption reaches 90% of the continuum, similar to the method outlined in Chisholm et al. (2015).

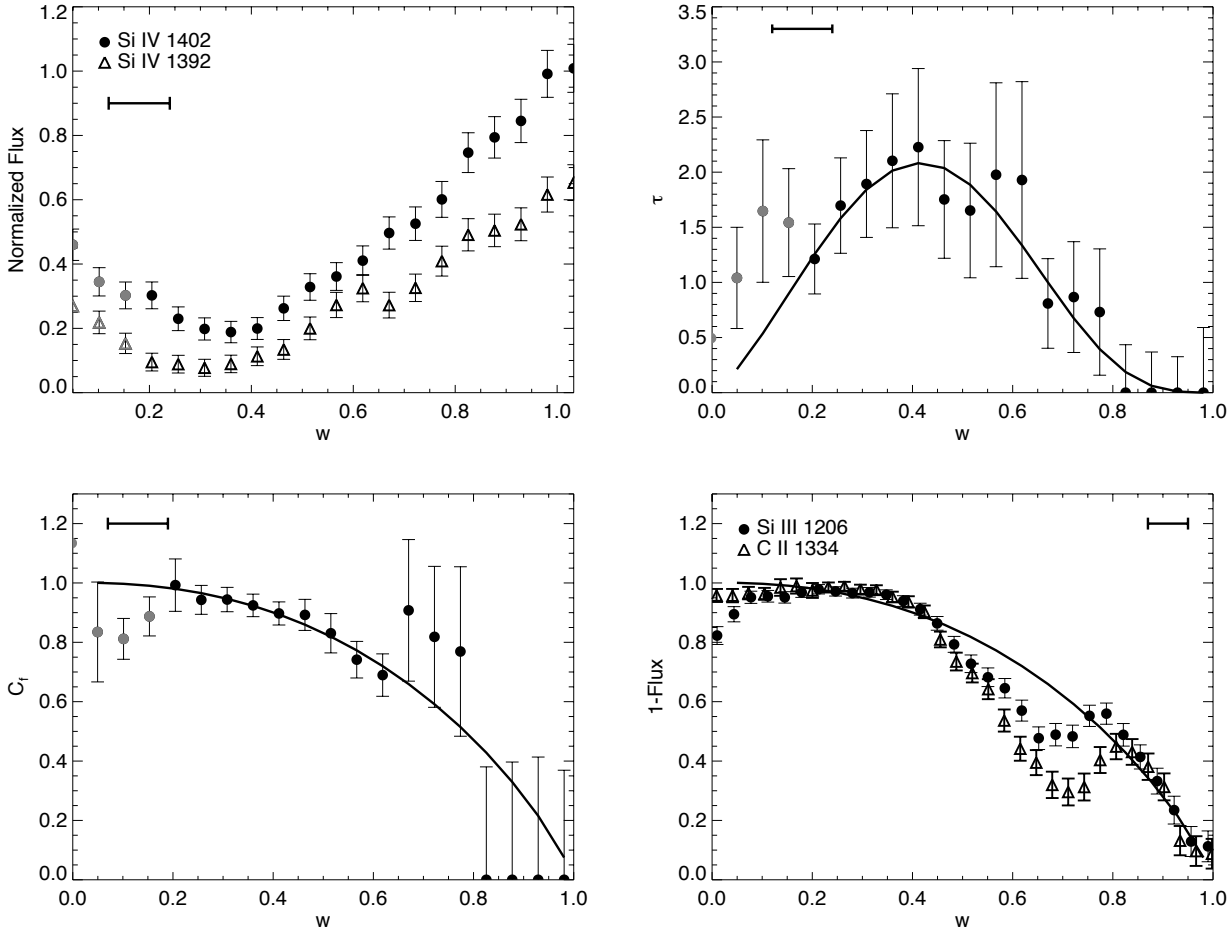

Figure 3. Normalized velocity (w = v/v$_\infty$; v$_\infty$ =-399 km s^{-1}) profiles of the Si IV 1402 Å absorption line. The upper left panel shows the absorption profiles of the Si IV 1402 Å (solid circles) and Si IV 1392 Å lines (open triangles). The upper right panel shows the variation of the Si IV 1402 Å optical depth (τ) with normalized velocity computed using the radiative transfer equation for the Si IV doublet (Equation 2). The lower panel shows the variation of the Si IV covering fraction (C$_f$; Equation 1) with normalized velocity. The black lines show the simultaneous best fit of Equation 12 for τ and C$_f$. Velocities less than 0.2 are excluded from the fits due to contributions from resonant emission and zero-velocity absorption (§ 2.3), and are plotted in gray. The best-fit parameters are given in Table 3. Lower right panel: velocity profile of 1-Flux, an approximation for C$_f$ for optically thick lines, for the Si III (circles) and C II (triangles) profiles. These two lines are amongst the strongest metal lines in the bandpass. The Si IV C$_f$ fit from the lower left panel is over-plotted, demonstrating that the Si IV C$_f$ fit is also a fair representation of the saturated lines. The velocity resolution (48 km s^{-1}) is given by a bar in the corner of each panel.

We must model how n$_4$ is distributed with radius. Previous studies assume that the density is either constant with velocity (Martin & Bouché 2009; Steidel et al. 2010), or that the density follows the continuity equation (Prochaska et al. 2011; Scarlata & Panagia 2015). However, to remain general we assume that the density follows a power-law scaling with radius, such that

$$\mathrm{n_4}(x) = \mathrm{n_{4,0}} x^{\alpha} \tag{5}$$

where n$_{4,0}$ is the Si IV density at the initial radius, R$_\mathrm{i}$. Placing this into Equation 4 gives the relation

$$\tau(x) = \frac{\pi e^2}{\mathrm{mc}} f \lambda_0 \frac{\mathrm{R_i}}{\mathrm{v_\infty}} \mathrm{n_{4,0}} x^{\alpha} \frac{dx}{dw} = \tau_0 x^{\alpha} \frac{\mathrm{d}x}{\mathrm{d}w} \tag{6}$$

where we have combined the constants into a single constant, τ_0, that represents the maximum optical depth.

Additionally, we derive the covering fraction of the Si IV absorption (C$_f$; see Equation 1). As we discuss in § 5.2, the covering fraction is the proportion, expressed as a percentage, of the starburst area covered by the outflow at a given radius. We assume that the covering fraction scales as a power-law with distance (as physically motivated in § 5.2), such that

$$C_f(w) = C_f(\mathrm{R_i}) \left(\frac{\mathrm{r}}{\mathrm{R_i}} \right)^{\gamma} = C_f(\mathrm{R_i}) x^{\gamma} \tag{7}$$

Now we have related the two observables of the profile to the distance from the starburst.

Equation 6 and Equation 7 are given in terms of distance, while we measure the parameters in terms of velocity. Many of the physical mechanisms for driving outflows scale the velocity with radius as a β velocity law (see § 5.3 below; Lamers & Cassinelli 1999), such that

$$\mathrm{v} = \mathrm{v}_{\infty}\left(1 - \frac{\mathrm{R_i}}{\mathrm{r}}\right)^{\beta} \tag{8}$$

Substituting for w and x, and inverting this relation gives the normalized radius in terms of the velocity as

$$x = \frac{1}{1 - w^{1/\beta}} \tag{9}$$

Taking the derivative of this gives the velocity gradient in terms of the normalized velocity and the β exponent as

$$\frac{\mathrm{d}x}{\mathrm{d}w} = \frac{w^{1/\beta - 1}}{\beta\left(1 - w^{1/\beta}\right)^2} \tag{10}$$

We can also use the β-law to derive the density scaling with velocity as

$$\mathrm{n}(w) = \mathrm{n}_{4,0}\left(\frac{1}{(1 - w^{1/\beta})}\right)^{\alpha} \tag{11}$$

producing an τ (Equation 6) and C_f (Equation 7) velocity scaling as

$$\begin{aligned} \tau\,(w) &= \tau_0 \frac{w^{1/\beta - 1}}{\beta(1 - w^{1/\beta})^{2+\alpha}} \\ C_f(w) &= \frac{C_f(\mathrm{R_i})}{(1 - w^{1/\beta})^{\gamma}} \end{aligned} \tag{12}$$

We then have five parameters to fit for: the maximum optical depth (τ_0), the covering fraction at the initial radius ($\mathrm{C}_f(\mathrm{R_i})$), the exponent of the beta velocity-law (β), the exponent of the density law (α), and the exponent of the covering fraction law (γ).

Using MPFIT (Markwardt 2009), we simultaneously fit for the five parameters from the unsaturated Si IV 1402 Å τ and C_f distributions (see Figure 3). At w below 0.2 ($v > -80$ km s^{-1}) zero-velocity absorption and resonance emission may effect the distributions (see § 2.3); therefore, we only fit the distributions between w of 0.2 and 1.0 (the points outside this range are coloured gray in Figure 3). The C_f and τ fits are shown in Figure 3, and the fit parameters are given in Table 3. In these fits we have binned the flux array by a factor of two (20 km s^{-1}) to increase the signal-to-noise ratio, while still Nyquist sampling the observed velocity resolution (see the bar in Figure 3). These fits reproduce the observed τ and C_f distributions, and describe the radial velocity and density laws of the outflow through Equation 8 and Equation 11. In § 5 we discuss some implications of these trends.

To test the covering fraction fits, we can use the Si III and C II profiles. Since these profiles are much stronger, they are strongly saturated at all velocities. This means that we cannot measure the C_f with the previous formula (Equation 1), while τ cannot be accurately measured at all. Rather, at large τ, the depth of the line is completely set by C_f, and is measured as $\mathrm{C}_f(\mathrm{v}) = 1 - F(\mathrm{v})$. In the lower right panel of Figure 3 we plot the C_f for Si III (circles) and C II (triangles). The Si IV C_f fit is over-plotted on these measurements and provides reasonable agreement with the data.

(1) τ_0	(2) β	(3) α	(4) $\mathrm{C}_f(\mathrm{R_i})$	(5) γ
4.80 ± 1.41	0.43 ± 0.07	-5.72 ± 1.51	1.00 ± 0.04	-0.82 ± 0.23

Table 3. Table of the quantities derived from the profile fits of the optical depth (τ) and covering fraction (C_f; see Equation 12). The individual parameters are: Column 1, τ_0, optical depth at line center; Column 2, β, the velocity power-law index; Column 3, α, the column density power-law index; Column 4, $\mathrm{C}_f(\mathrm{R_i})$, the maximum covering fraction; Column 5, γ, the covering fraction power-law index.

4 IONIZATION MODELLING

In § 2.4 we calculate the integrated column density (N) for individual metal ions, but these only describe the individual ion and not the total mass of the outflow. While Ly-α absorption traces the neutral Hydrogen in the outflow, we opt to use the metal lines to describe the outflow because (1) the strong P-Cygni Ly-α profile requires detailed radiative transfer models to constrain (Verhamme et al. 2006) and (2) up to 99% of the Hydrogen in the outflow may be ionized (Chisholm et al. 2016). To calculate the total Hydrogen in the outflow, ionization models are required to measure the ionization fraction (χ_i, or the fraction of the total gas within transition i) and the abundance ($\mathrm{N_i/N_H}$, or the ratio of an element to the total Hydrogen).

In Chisholm et al. (2016) we find that photoionization models describe the ionization structure of galactic outflows. These models require the outflow metallicity ($\mathrm{Z_o}$) to be greater than 0.5 $\mathrm{Z_\odot}$ and the ionization parameter (log(U); the ratio of the photon density to outflow density) to be between -1.5 and -2.25. Additionally, the ionization structure depends both on the spectral energy distribution and the strength of the ionizing source, as well as the density ($\mathrm{n_0}$) of the outflow.

We model the ionization structure using CLOUDY version 13.03 (Ferland et al. 2013). The CLOUDY models are not velocity resolved profiles, rather we are fitting the measured integrated column densities to the integrated values from CLOUDY. We assume that the outflow is ionized by the observed stellar continuum, using the best-fit STRABURST99 stellar continuum model from § 2.2. These STARBURST99 models have an age of 4.478 Myr and a constant SFR of 25.15 $\mathrm{M_\odot\ yr^{-1}}$ (see Table 1). In the CLOUDY models, we assume an expanding spherical geometry, which is not meant to reproduce the velocity profiles, but to account for back-scattering of radiation. We set the covering fraction to 1.00, the observed value from the Si IV transition, and scale the density with a power-law of -5.72, as measured above. The CLOUDY models are stopped once the simulations reach 3000 K, which is lower than the default criteria to allow for higher metallicities. These lower temperatures require a cosmic ray background to be included (Indriolo et al. 2007).

We use CLOUDY's default H II abundances, which are similar to the Milky Way values (Baldwin et al. 1991; Savage & Sembach 1991; Osterbrock et al. 1992; Rubin et al. 1993), and include an Orion Nebular dust grain distribution (Baldwin et al. 1991). The dust grains account for scattering and destruction of photons, as well as depletion of metals onto

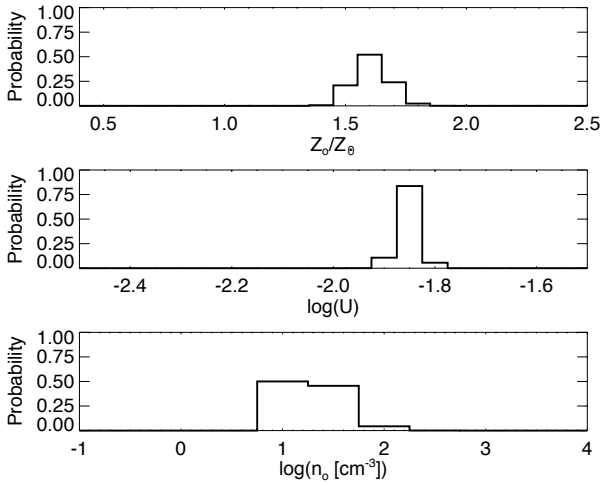

Figure 4. Probability density functions (PDFs) from the CLOUDY ionization modelling. The three parameters are outflow metallicity (top panel), ionization parameter (middle panel), and the total Hydrogen density at the initial radius (bottom panel). The PDFs are single peaked, with expectation values and standard deviations given in Table 5.

grains. The abundances are scaled by a constant factor to change the outflow metallicity (Z_o). Similarly, we vary the outflow density at the inner radius (n_0), ionization parameter (U), and the stellar continuum metallicity (Z_s).

We use a Bayesian approach to estimate Z_o, n_0, U, and Z_s (Kauffmann et al. 2003; Brinchmann et al. 2004; Feigelson & Jogesh Babu 2012). While Chisholm et al. (2016) uses the W ratios to define the ionization structure, the relatively high signal-to-noise ratio and spectral resolution observations of NGC 6090 allow us to use the measured column densities from four weak transitions: O I 1302Å, Si II 1304Å, S II 1250Å, and Si IV 1402Å (see Table 2). We do not use the N V column densities due to Milky Way C I1277Å and imperfect continuum subtraction contamination near the N V line (see § 2.2). We create grids of CLOUDY models, with differing input parameters (Table 4), and tabulate the predicted CLOUDY column densities. We assume a uniform prior – each model is equally likely – and compute the likelihood function of each set of parameters as

$$\mathrm{L} \propto \exp(-\chi^2/2). \quad (13)$$

where χ^2 is the chi-squared function using the observed column density (N), the errors on the observed N, and the predicted N from CLOUDY. For each parameter (Z_o, n_0, U, and Z_s), the likelihood function is marginalized over the other nuisance parameters and normalized to one to create probability distribution functions (PDFs). We calculate expectation values and standard deviations of the individual parameters from these PDFs as estimates of the parameters, and their uncertainties.

We do the fitting in two iterations. The first iteration uses a course grid to determine the best Z_s. Since there are only five stellar continuum metallicities in the fully theoretical STARBURST99 models, we only coarsely estimate the stellar continuum metallicity. Similar to the COS spectrum fitting (see § 2.2), the Bayesian analysis finds that the 1 $Z_\odot$ model best fits the ionization structure, assigning 100% of the probability to the 1 $Z_\odot$ stellar continuum model.

Parameter	Range	Step Size	Number of Steps
log(U)	(-2.5, -1.5)	0.05	21
$Z_o/Z_\odot$	(0.4, 2.5)	0.1	22
log(n_0)	(-1, 4)	0.5	11

Table 4. Grid of CLOUDY models used in the Bayesian analysis of the ionization structure.

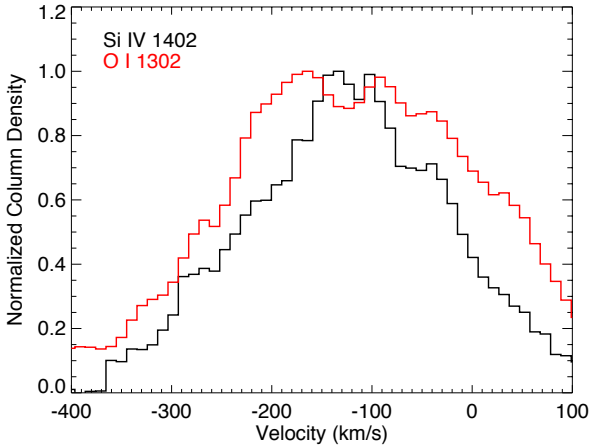

Figure 5. The velocity resolved column density plots for the Si IV (black) and O I (red) lines, normalized to their maximum values. The velocity structure between the neutral (O I) and highly ionized gas (Si IV) stays roughly constant over the velocity range, implying that the ionization structure does not vary substantially with velocity.

The second iteration uses a more finely spaced grid for Z_o, log(U) and n_0, while only using the solar metallicity stellar continuum model (see Table 4). In Figure 4 we show the PDFs for the three parameters, with narrow distributions that have expectation values of $Z_o = 1.61 \pm 0.08$ $Z_\odot$, $n_0 = 18.73 \pm 2.37$ cm^{-3}, and log(U)$= -1.85 \pm 0.02$ (see Table 5). Using these parameters, we create a best-fit CLOUDY model, producing the ionization fractions of the outflow (see Table 5). As discussed in § 5.1, these ionization models have important implications for the metallicity of the outflow, the inner radius of the outflow, and the mass outflow rate.

4.1 Ionization Structure With Velocity

In the following analysis we use an integrated ionization correction. However, if the outflow is heated as it is accelerated, then the column density ratio of high to low ionization potential lines should increase with velocity. Figure 5 shows the velocity resolved column densities for the Si IV and O I transitions, showing that there is not a coherent variation of the column densities with velocity between -400 and 0 km s^{-1}. This implies that a majority of the column density arises from a small radius, and the photoionization models are approximately plane-parallel.

Row Number	Property	Value
(1)	log(U)	-1.85 ± 0.02
(2)	$Z_o/Z_\odot$	1.61 ± 0.08
(3)	$Z_s/Z_\odot$	1.0
(4)	n_0 [cm^{-3}]	18.73 ± 2.37
(5)	$\chi_{Si\ IV}$	$0.087^{+0.004}_{-0.002}$
(6)	log(Si/H)	-5.19±0.02
(7)	log($N_{Si\ IV}$) [log(cm^{-2})]	14.64 ± 0.04
(8)	log(N_H) [log(cm^{-2})]	$20.89^{+0.04}_{-0.03}$
(9)	R_i [pc]	63.4
(10)	T_H [K]	5470

Table 5. Table of the quantities derived from the CLOUDY photoionization modelling. Row (1) is the ionization parameter; (2) is the derived outflow metallicity; (3) is the stellar continuum metallicity; (4) is the Hydrogen density at the base of the outflow; (5) is the ionization fraction of Si IV, or the per cent of the total Si in the Si IV transition; (6) The best-fit Si to H abundance value; (7) The measured Si IV column density; (8) The total Hydrogen column density calculated from the Si IV column density, Si/H abundance, and the Si IV ionization fraction; (9) The inner radius, calculated using Equation 15; (10) the H II temperature of the best-fit CLOUDY model. The errors on χ_{SiIV} and log(Si/H) are calculated by producing CLOUDY models of the estimate plus/minus 1σ errors of the Z_o, n_0, and log(U).

5 DISCUSSION

Here we discuss various aspects of the profile and ionization fitting from § 3 and § 4. In § 5.1, we first derive important parameters of the outflow. We then study the implications for the covering fraction (§ 5.2), velocity (§ 5.3), and density (§ 5.4) radial scalings. Finally, we combine the various relations to determine the mass outflow rate of NGC 6090 (§ 5.5).

5.1 Ionization Modelling

With the ionization fractions and metallicities derived in § 4, we convert the measured Si IV column densities into a total Hydrogen density (see Table 5). The total (neutral plus ionized) Hydrogen column density is $20.89^{+0.04}_{-0.03}$ cm^{-2}, where the uncertainties for each parameter are propagated to compute the uncertainties of the total Hydrogen column density. The UV continuum extinction provides a complimentary way to estimate the total Hydrogen column density by relating the extinction to the amount of dust through a dust-to-gas ratio. We use the relation from Leitherer et al. (2002) and Heckman et al. (2011) to calculate the total Hydrogen column density as

$$N_H = \frac{3.6 \times 10^{21} E(B-V)}{Z} cm^{-2} \quad (14)$$

where we use a starburst dust attenuation law and the relation for the FUV optical depth from Gil de Paz et al. (2003) to convert the spectral slope to E(B-V). Using the extinction measured from the UV continuum in Chisholm et al. (2016) and the outflow metallicity from the ionization structure (see Table 1 and Table 5), we expect a log(N_H) of 20.85, in agreement with the derived total N_H from the ionization modelling.

The ionization model predicts that 99.3% of the Hydrogen in the outflow is ionized. These low neutral fractions suggest that the outflow has a H I column density of 5×10^{18} cm^{-2}. Current radio arrays cannot detect this H I column in emission, but the upcoming SKA will detect these densities with 10.″0 spatial resolution and 5 km s^{-1} spectral resolution in 10-100 hours of integration time (de Blok et al. 2015).

The outflow metallicity is 1.61 $Z_\odot$, 61% and 34% larger than the measured stellar and ISM metallicities (see Table 1). Substantial uncertainties on log(O/H) measurements (Kewley et al. 2006) means that the outflow metallicity is at least consistent with the ISM values, and likely enriched compared to the ISM of the galaxy. Additional metals may reside in a hotter phase not probed by these observations (see below for a discussion of this phase). Metal enriched outflows are important constraints for models using galactic outflows to explain the mass-metallicity relation (Tremonti et al. 2004; Finlator & Davé 2008; Peeples & Shankar 2011; Creasey et al. 2015; Christensen et al. 2015). For example, to match the mass-metallicity relation of Denicoló et al. (2002) for galaxies with log($M_*/M_\odot$) of 10.7, Figure 8 of Peeples & Shankar (2011) suggests that the outflow metallicity is 1.58 $Z_\odot$. The same figure also uses Z_o to constrain the scaling of the mass outflow rate divided by the star formation rate (mass-loading factor). In future studies, we will determine the scaling of the outflow metallicity with stellar mass and star formation rate to better constrain these studies.

The initial radius (R_i) can be determined from the fitted Si IV optical depth (see Equation 6). Solving for R_i in terms of the observed maximum Si IV optical depth, we find that

$$R_i = \frac{mc}{\pi e^2} \frac{1}{f\lambda} \frac{v_\infty \tau_0}{n_0 \chi_{Si\ IV} Si/H} = 63.4 \text{ pc} \quad (15)$$

Using the values from the β-profile fitting (Table 3) and the ionization modelling (Table 5). We have related the initial Si IV density ($n_{4,0}$) to the Hydrogen density at the base of the outflow, the abundance, and the ionization corrections from the ionization models ($n_{4,0} = n_0 \chi_{SiIV} Si/H$). The inner outflow radius and the size of the mass-loading region (maximum extent of about 150 pc; see § 5.5 and Figure 10 below) is consistent with models of the mass-loading region in M 82 (**?**Strickland & Heckman 2009), and with analytical work from Heckman et al. (2015), who assume that the inner outflow radius is twice the size of the starburst. However, what is the physical meaning of the inner outflow radius?

The shredding of supernovae blastwaves by hydrodynamical instabilities is a possible origin for this inner radius. Supernovae energy builds up in the ISM due to multiple impulsive events (**?**), which creates a blastwave that shocks when it encounters the ambient ISM (Taylor 1950; Sedov 1959; Weaver et al. 1977; McKee & Ostriker 1977; Ostriker & McKee 1988; Kim & Ostriker 2015). The shock compresses surrounding ISM into a thin, dense shell of relatively cool gas that travels outward. This phase is called the snowplow phase, and the radius depends on the amount of injected energy, the density of the medium, and how much of the energy is radiated away (Weaver et al. 1977; McKee & Ostriker 1977; Cooper et al. 2008; **?**; Kim & Ostriker 2015), with typical values near 20-30 pc (Draine 2011; Kim & Ostriker 2015).

Once the shell forms, Rayleigh-Taylor and Kelvin-Helmholtz instabilities rapidly destroy it, creating many small warm (10^4 K) cloudlets (Mac Low et al. 1989; Cooper

et al. 2008; Fujita et al. 2009; Martin & Bouché 2009; **?**; Thompson et al. 2016). The destruction of the blastwave allows the hot interior gas to escape and travel into the halo as a hot wind. The hot, high-velocity wind, may then accelerate these clouds through ram pressure to the observed velocities (Fujita et al. 2009; Martin & Bouché 2009; Thompson et al. 2016). Therefore, a possible origin for R_i is that hydrodynamic instabilities have shredded the dense blastwave, and injected cloudlets into the hot wind.

Finally, the CLOUDY modelling estimates the temperature of the H II in the outflow to be 5470 K (see Table 5), leading to a pressure of $P/k_b = 1 \times 10^5$ K cm^{-3}. The hot wind is typically assumed to have a temperature of 10^7 K (Chevalier & Clegg 1985). If the observed cloudlets and hot wind are in pressure equilibrium, then the hot wind has a density of 0.01 cm^{-3} at R_i, a factor of 10 lower than the density in the Chevalier & Clegg (1985) model. However, recent models by Bustard et al. (2016) show that the density and temperature of this hot wind can greatly vary, depending on the efficiency and mass-loading of the outflow.

Regardless of the origin of the outflow, it must be evenly distributed across the stellar continuum to produce a unity covering fraction (see Table 3). However, the external pressure on the outflow decreases as it accelerates out from the starburst. The change in pressure has a dramatic effect on the size of the cloudlets in the outflow, and in turn their covering fraction. In the next section we discuss this pressure change, and how it naturally leads to the observed scaling of the covering fraction with velocity.

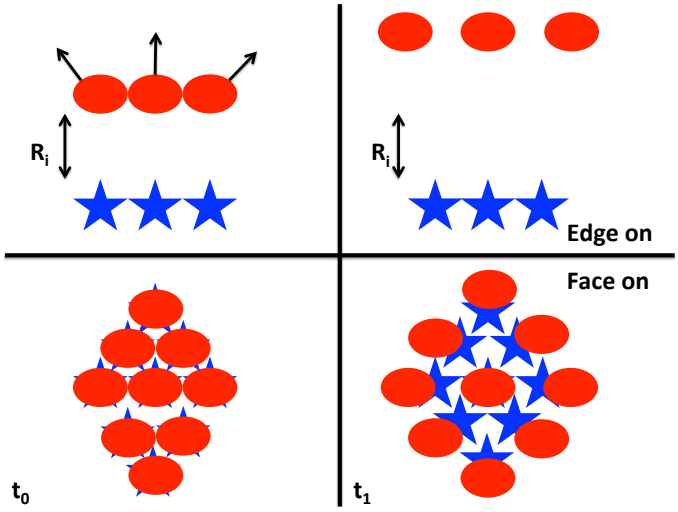

Figure 6. Upper panels: Edge on cartoon of outflowing cloudlets (red circles). At an initial time, t_0, (left panels) the clouds start a distance, R_i, from the starburst (blue stars). At t_0, these clouds completely cover the background stars (see face on view in the lower left panel), and the stellar continuum is not transmitted. The clouds are accelerated away from the starburst until a later time, t_1 (right panels). We assume that these clouds maintain their size, and gaps are created between the cloudlets as they move away from the starburst. When viewed face on (lower right), the gaps expose the background starburst, reducing the covering fraction as x^{-2} (see text).

5.2 Covering Fraction

In § 3, we observe that the outflow initially completely covers the background stellar continuum, but as the velocity increases the outflow covers less of the background stars (C_f drops as $x^{-0.8}$). To physically understand this scaling relation, we hypothesize that the absorption arises from cloudlets of gas initially a distance R_i from the starburst (see the upper left panel of Figure 6). At R_i these clouds are large enough to completely occupy the volume along the line-of-sight to the stars: none of the stellar continuum is transmitted (see lower left panel in Figure 6 for the face on view at the initial time, t_0). However, the starburst imparts energy and momentum to these clouds, accelerating them radially outwards (upper right panel of Figure 6).

In the simplest scenario, these clouds retain their size as they move outward, and a gap appears between the clouds (see upper right panel in Figure 6). The gap allows the background stellar continuum to be transmitted, reducing the covering fraction of the stellar continuum. This is illustrated by the face on view in the lower right panel of Figure 6, where background stars become visible in the gaps between the clouds at higher velocities.

This physical picture can be expressed numerically as a ratio of the cloud area to the total surface area at a given radius (r) as (Martin & Bouché 2009)

$$\frac{C_f(r)}{C_f(R_i)} = \frac{A_c(r)}{4\pi r^2}\frac{4\pi R_i^2}{A_c(R_i)} = \frac{A_c(r)}{A_c(R_i)}x^{-2} \quad (16)$$

Where A_c is the area of the individual cloudlets and $x = r/R_i$. Assuming that the area of the clouds remains constant, the C_f in this scenario scales as x^{-2}, significantly steeper than the observed relation of $x^{-0.8}$.

However, this simple model of static clouds is not the most physical. These cloudlets are likely in pressure equilibrium with an external pressure ($P_e = P_c$, where P_e is the external pressure and P_c is the pressure of the cloud), possibly a hot wind (see Figure 7 and the discussion in § 5.1). Changes in P_e change P_c, and the clouds expand adiabatically to account for these changes as $P_c \propto V_c^{-\gamma_c}$, where V_c is the volume of the clouds and γ_c is the adiabatic index (5/3 for monatomic ideal gas). The larger cloud volume reduces the gap between the individual cloudlets (Martin & Bouché 2009). The lower right panels of Figure 6 and Figure 7 illustrate that the larger clouds cover more of the background stars than the static clouds do, and C_f falls more slowly with distance.

Approximating the outflow as spherical clouds provides a relation for A_c in terms of the volume of the cloudlets as $A_c \propto V_c^{2/3}$. Using this approximation, Equation 16, and the observed C_f ($C_f \propto x^{-0.8}$), the cloud volume changes with distance from the starburst as

$$\frac{V_c(r)}{V_c(R_i)} = \left(\frac{A_c(r)}{A_c(R_i)}\right)^{3/2} = \left(\frac{C_f(r)}{C_f(R_i)}x^2\right)^{3/2} = x^{1.8\pm0.4} \quad (17)$$

This demonstrates that the cloud's volume increases with distance from the starburst, but what differential pressure is needed to change the volume as we observe?

Here, we consider two different pressure laws for a mass-conserving external medium: isothermal expansion and adiabatic expansion. If the external pressure changes isother-

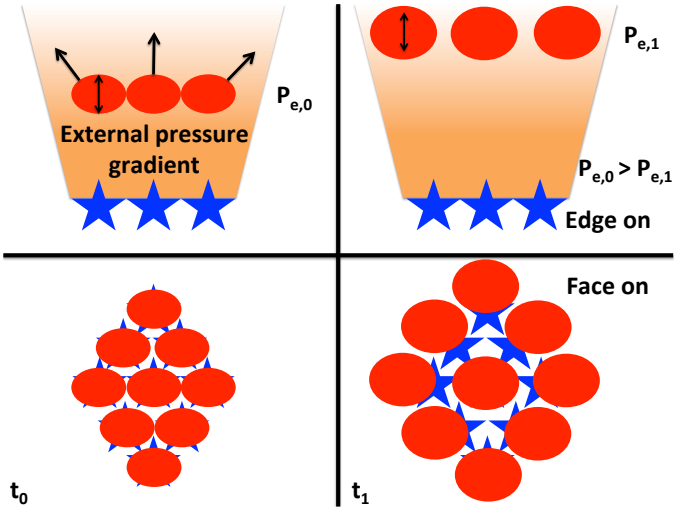

Figure 7. Similar to Figure 6, but the clouds are in an external pressure gradient (orange shaded region). The initial pressure ($P_{e,0}$) is greater than the pressure at t_1 ($P_{e,1}$). The cloudlets adiabatically expand to remain in pressure equilibrium with the external medium (see the arrow in the upper left cloud demonstrating it's initial diameter). Comparing the bottom right panel with the same panel in Figure 6, the expanded clouds now cover more area of the starburst at higher velocities. This slows the drop in C_f. The scaling of the C_f with distance depends on how the external medium changes, either isothermally (see Equation 19) or adiabatically (see Equation 20).

mally with radius then $P_e(r)/P_e(R_i) = x^{-2}$. Assuming that the spherical clouds and the isothermal external medium remain in pressure equilibrium ($P_c = P_e$), the pressure of the outflowing clouds changes as

$$\frac{P_c(r)}{P_c R_i} = \left(\frac{V_c(r)}{V_c(R_i)}\right)^{-\gamma_c} = \left(\frac{A_c(r)}{A_c(R_i)}\right)^{-3\gamma_c/2} = x^{-2} \quad (18)$$

Solving for $\frac{A_c(x)}{A_c(R_i)}$ in terms of x finds that A_c changes as $x^{4/(3\gamma_c)}$. Placing this into Equation 16 gives the C_f scaling of

$$\frac{C_f(r)}{C_f(R_i)} = x^{4/(3\gamma_c)} x^{-2} = x^{-1.2} \quad (19)$$

For a $\gamma_c = 5/3$. If the clouds expand adiabatically while immersed in an isothermal external medium, the covering fraction declines less steeply with height than if the clouds maintain their initial size.

Equation 19 is still too steep to match the observed scaling. Another possibility is that the external pressure changes adiabatically. In this situation $P_e \propto x^{-2\gamma_e}$, where γ_e is the adiabatic index of the external medium. Following a similar process as above, the covering fraction of an adiabatically expanding outflow in pressure equilibrium with an adiabatically expanding external medium is (Martin & Bouché 2009)

$$\frac{C_f(r)}{C_f(R_i)} = x^{4\gamma_e/(3\gamma_c)-2} = x^{-2/3} \quad (20)$$

where we have assumed that γ_e and γ_c are equal to each other (i.e. both the clouds and external medium are monatomic ideal gases). Interestingly, since diatomic gas has more degrees of freedom than monatomic gas, diatomic gas requires a larger energy change to remain in pressure equilibrium, as seen by the smaller γ_c of diatomic gas (7/5). Using Equation 20, we find that molecular clouds expand more rapidly, and consequently have a more gradually declining C_f with distance, as $x^{-0.4}$. This has an important consequence for the survival of molecular clouds in a hot medium. By increasing the radius of the cloud, it takes longer for a shock wave to propagate across the cloud and dissociate the molecular gas (Klein et al. 1994; Scannapieco & Brüggen 2015). This may extend the lifetime of molecular gas entrained in galactic outflows, while the increased C_f may explain the presence of molecular gas at high velocities (Matsushita et al. 2000; Sakamoto et al. 2014; Leroy et al. 2015).

In § 3, we find that the covering fraction scales as $C_f = 1.0\ x^{-0.8\pm0.2}$, in agreement with the adiabatic expansion of cloudlets in an adiabatically expanding external medium (Equation 20). However, it is an interesting theoretical question whether clouds can remain in pressure equilibrium with an external medium and still be accelerated. Ram pressure introduces a secondary pressure term, but if the clouds are shielded from direct interaction with the hot medium then the pressure of the cloud is set by the external thermal pressure (Chevalier & Clegg 1985). Further, ablation and ram pressure stripping create a fractal distribution into smaller cloudlets (Klein et al. 1994; Scannapieco & Brüggen 2015), which may produce the observed change in covering fraction. The velocity scaling of the covering fraction provides further constraints for simulations of the acceleration of clouds. The acceleration of the cloudlets out of the star forming region decreases C_f, but how are the clouds accelerated?

5.3 Velocity Law

The velocity law describes the acceleration of the outflowing clouds with distance. In § 3 we find a β velocity profile of $v(r) = v_\infty\ (1 - \frac{R_i}{r})^{0.43\pm0.07}$. The outflow initially accelerates rapidly, but the acceleration moderates at large radii (see the black line in Figure 8). Using the initial radius calculated in § 5.1, the outflow reaches 50% (90%) of the maximum velocity in 79 pc (291 pc). Acceleration much beyond this is not well constrained by the data.

Outflows typically have a "saw-tooth" line profile (Weiner et al. 2009), where the red side of the profile sharply declines and the blue side rises gradually. The velocity and C_f laws produce these profiles. Initially, the velocity sharply increases over a short distance, keeping the C_f near unity because C_f scales as $x^{-0.82}$. Meanwhile, at higher velocities the clouds travel larger distances per velocity interval, forcing the high-velocity clouds to expand to remain in pressure equilibrium with the adiabatically expanding external medium. This moderates the decline in C_f, and produces the gentler rising blue portion of the profile.

The observed Si IV 1402Å outflows do not escape the galactic potential. Following Heckman et al. (2000), the escape velocity is no more than three times the circular velocity (136 km s^{-1}; Chisholm et al. 2015), therefore the outflow velocity needs to exceed 651 km s^{-1} for the clouds to escape the potential. There are two possible explanations for why we do not observe gas escaping the potential: (1) the outflow does eventually exceed the escape velocity but the Si IV density drops below the detection limits at high velocities and

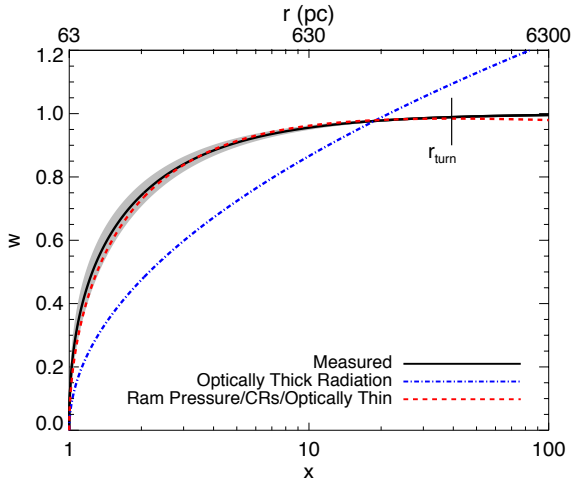

Figure 8. Normalized velocity ($w = v/v_\infty$; $v_\infty = -399$ km s^{-1}) profile with normalized radius ($x = r/R_i$; $R_i = 63.4$ pc, see Equation 15). The solid black curve represents the measured β velocity law from § 3, while the grey shaded region corresponds to the fitted error on β. The blue dot-dashed and red dashed lines represent theoretical velocity profiles of optically thick radiation pressure and ram pressure/cosmic ray/optically thin radiation pressure (any r^{-2} force in opposition with gravity) driven outflows, respectively. The upper x-axis is given in terms of pc, as measured in § 5.1. At 2.5 kpc the r^{-2} profile begins to decelerate, and this radius (r_{turn}) is marked by a vertical line.

we do not observe the escaping gas (see § 5.4) or (2) the outflow does not actually escape the galaxy, but rather recycles back into the disc as a galactic fountain (Shapiro & Field 1976). The latter is consistent with Chisholm et al. (2015), which finds most galaxies with $\log(M_*/M_\odot)$ greater than 10.5 cannot drive outflows faster than their escape velocity, unless they are undergoing a merger. Observations probing lower density gas, such as Lyman-α, may constrain whether these outflows are capable of escaping the gravitational potential.

Now we study how these outflows are accelerated. There are numerous theoretical ways to accelerate galactic outflows: radiation pressure on dust grains (Thompson et al. 2005; Murray et al. 2005), cosmic rays (Everett et al. 2008; Socrates et al. 2008), and ram pressure of a hot wind on the cloudlets (Murray et al. 2005; Cooper et al. 2008; Fujita et al. 2009; Martin & Bouché 2009). Below, we use analytical expressions for how the velocity profile evolves radially to explore which mechanisms could accelerate these outflows. In each case, we give the scaling of the normalized velocity ($w = v/v_\infty$; where v_∞ is the maximum velocity) with the normalized radius ($x = r/R_i$; where R_i is the initial radius). We then scale the analytical expressions to the observed relations to determine the plausibility of each mechanism. In § 5.3.3 we summarize the implications for the theoretical profiles.

5.3.1 *Optically Thick Radiation Pressure*

Radiation pressure is an attractive way to drive outflows in dusty, vigorously star-forming galaxies: the high luminosity provides a large momentum source (Murray et al. 2005), while the large dust optical depth scatters photons multiple times (Thompson et al. 2005). Murray et al. (2005) give the radial scaling of the velocity for optically thick radiation pressure as:

$$w = \sqrt{\frac{4\sigma^2}{v_\infty^2}\left(\frac{L}{L_E} - 1\right)\ln(x)} \tag{21}$$

where σ is the velocity dispersion of the galaxy, L is the luminosity of the galaxy, and L_E is the Eddington luminosity. We fit for the constant value that best matches the observed β-law using MPFIT (Markwardt 2009), while excluding velocities less than 0.2. The fit is shown by the blue dot-dashed line in Figure 8. The optically thick radiation model poorly matches the observations.

5.3.2 *An r^{-2} Force*

A second appealing driving mechanism is ram pressure. Supernovae thermalize ambient gas into a hot wind, which expands adiabatically out of the star forming region. The hot wind imparts a ram pressure force on the clouds, which depends on the speed and density of the hot wind and the area of the cloud as $F_{ram} = \rho_h v_h^2 A_c$ (Klein et al. 1994; Scannapieco & Brüggen 2015). $F_{ram} \propto x^{-2}$ in a simplified case of a mass conserving, adiabatically expanding hot wind. Ram pressure driving is appealing because the C_f scaling is consistent with clouds being in pressure equilibrium with a adiabatically expanding external medium (§ 5.2), a situation that could lead to ram pressure driving. Including the effects of gravity, Murray et al. (2005) calculate the velocity profile of a ram pressure driven outflow as

$$w(x) = \sqrt{\frac{v_c^2}{v_\infty^2}\left(1 - \frac{1}{x}\right) - \frac{4\sigma^2}{v_\infty^2}\ln(x)} \tag{22}$$

Where v_c, the characteristic velocity clouds reach before gravity dominates, is defined as $v_c = \frac{3\dot{M}_h V_h}{8\pi\rho_c R_c R_i}$. Defining A as v_c^2/v_∞^2 and B as $4\sigma^2/v_\infty^2$, we fit for the values of A (fitted value of 1.10) and B (fitted value of 0.03) that match the observed β velocity law, as shown by the red line in Figure 8.

Similarly, shockwaves from supernovae accelerate cosmic rays (CR). These relativistic particles stream out of the star forming regions along the magnetic fields and exchange momentum with magnetized plasma. Cosmic rays have various advantages over radiation pressure and ram pressure, including: CRs interact multiple times with the gas, magnetic fields confine CRs to the galaxy making it difficult for CRs to escape without imparting momentum, and CR feedback is independent of the distribution of ISM gas (Everett et al. 2008; Socrates et al. 2008). Socrates et al. (2008) derive the force imparted by cosmic rays as

$$F_{CR} = \frac{\kappa_{CR}}{c}\frac{L_{CR}}{4\pi r^2} \tag{23}$$

where κ_{CR} is the cosmic ray opacity, and L_{CR} is the cosmic ray luminosity. This force produces a similar velocity scaling as the ram pressure scaling in Equation 22.

Additionally, the scaling of the ram pressure and CR velocity profiles are similar to an optically thin radiation profile (Murray et al. 2005). In fact, Equation 22 is a general form for any r^{-2} force that opposes gravity. Therefore, the red dashed line in Figure 8 corresponds to outflows driven

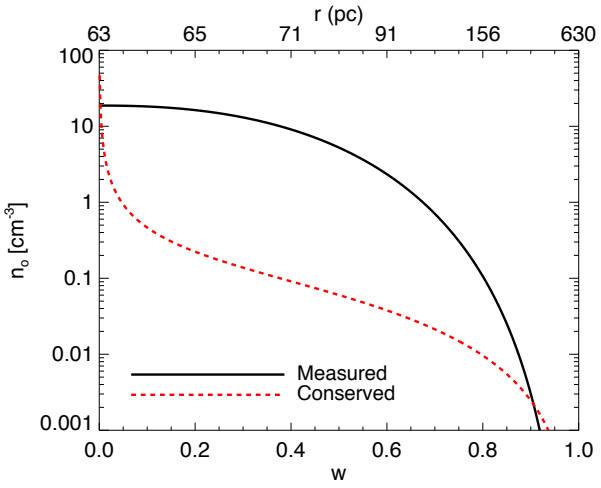

Figure 9. The measured outflow Hydrogen density scaling with normalized velocity ($w = v/v_\infty$) on the lower x-axis and radius on the upper x-axis. The density does not change appreciably at low velocities because the velocity rapidly increases over a short distance from the starburst (see Figure 8). At higher velocities the β-law flattens, and increases in velocity are accompanied by larger increases in radius. The red dashed line shows the density approximation of a mass-conserving flow with the observed velocity law (Equation 24). In a mass conserving flow, the density rapidly decreases at low velocity as the outflow is accelerated. Note that the density profile is only fit to the observations for $w > 0.2$. The radius formally extends to infinity, but the last tick corresponds to the radius of $r/R_i = 10$.

by any r^{-2} force (ram pressure, cosmic rays, or optically thin radiation pressure), and we cannot distinguish these mechanisms from the measured velocity profile.

5.3.3 Velocity Summary

The ram pressure, cosmic rays, and optically thin radiation pressure velocity profile (any r^{-2} force) matches the observed velocity relation for all observed velocities, while optically thick radiation pressure poorly matches the observed velocity profile (Figure 8). In Figure 8, the r^{-2} profile begins to decelerate at a radius of 2.5 kpc (r_{turn}; marked by the vertical line in Figure 8). However, at these large radii the outflow is now diffuse, and the deceleration of the outflow is challenging to study with the Si IV line profile.

5.4 Density Law

In § 3 we find the density to scale with the normalized radius as $n(x) \propto x^{-5.72}$. In Figure 9 we show the measured relation for the outflow density with velocity. At low velocities, the density remains nearly constant because the outflow accelerates over a short distance (Steidel et al. 2010), but at higher velocities the density precipitously drops. Stronger transitions probe lower densities than weaker transitions, causing stronger transitions to probe higher velocities than the weaker transitions. Therefore, stronger transitions have larger measured terminal velocities and larger line widths (because they probe a wider velocity distribution) than the weaker transitions (see Table 2; Grimes et al. 2009; Chisholm et al. 2016).

This density-velocity scaling implies that the outflow traced by Si IV does not conserve mass. Fitting the τ distribution with a mass-conserving flow produces a poor fit because the τ distribution declines sharply at high velocity. In the continuity equation, the mass flux is conserved, such that the density scales as

$$n(w) \propto \frac{n_0}{x^2 v} \propto \frac{n_0}{v_\infty} \frac{(1 - w^{1/\beta})^2}{w} \quad (24)$$

In Figure 9 we compare the mass-conserving density profile (red dashed line) with the observed profile. Compared to the observed density profile, the density of a mass-conserving flow rapidly decreases at low velocities as the outflow accelerates over small distances, while at higher velocities the conserved density decreases more gradually because the velocity gradient is flatter (see Figure 8).

If the Si IV flow is not mass-conserving, what happens to the Si IV gas? The density could decrease by: (1) increasing the volume of the outflowing clouds while keeping the number of Si IV ions constant or (2) decreasing the number of Si IV ions in the clouds. Equation 17 shows that the volume of the outflowing clouds scales as $x^{1.77}$, implying that the number of Si IV ions in the outflow must decrease as $x^{-3.95}$ to satisfy the observed density relation. One possibility is that the outflowing clouds lose mass through ablation, ram pressure stripping, or conduction from the hot wind (Klein et al. 1994; Scannapieco & Brüggen 2015; Zhang et al. 2015; Brüggen & Scannapieco 2016). In this scenario, the hot wind rapidly destroys the clouds and incorporates them into the hot wind, making the mass undetectable through Si IV absorption at higher velocities.

A steep density scaling relation is also seen in the nearby starburst M 82. Leroy et al. (2015) probe the surface density profiles of the molecular, neutral and ionized phases of the outflow from M 82. They find that only the H I follows an $n \propto r^{-2}$ density law largely because of the large amount of tidal material present at large radii. However, other surface density profiles along the minor axis decrease more rapidly. The 70 μm emission, a tracer of warm dust, and CO emission, a tracer of diffuse molecular gas, scale with the distance from the starburst as $n \propto r^{-4}$ (Leroy et al. 2015), roughly consistent, with the density scaling found here. The authors use the divergence of the density profile to argue that the outflow of M82 is a galactic fountain, with gas leaving the outflow and recycling back into the disk.

5.5 Mass Outflow Rate

Finally, we combine all of the derived relations to measure the mass outflow rate ($\dot{M}_o = dM_o/dt$) of the photoionized galacitc outflow. The photoionized outflow is a single component of the outflow, and other, unexplored, phases likely contribute to the total mass outflow rate. Since the hot phase is such low density, this photoionized phases likely dominates the mass budget of the outflow.

Typically the mass outflow rate is calculated assuming the outflow is in a thin spherical shell as

$$\dot{M}_o = \Omega C_f \mu m_p N_H r v_{cen} \quad (25)$$

where μm_p is 1.4 times the mass of the proton, Ω is the

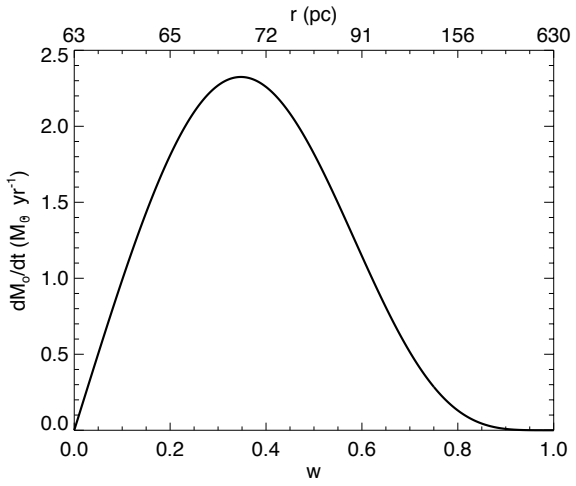

Figure 10. The mass outflow rate ($\dot{M}_o$ = dM$_o$/dt) of NGC 6090 with normalized velocity ($w = v/v_\infty$) on the lower axis, and radius, in pc, on the upper axis. The $\dot{M}_o$ is calculated using Equation 26, the fitted velocity profile, density profile, covering fraction profile, metallicity, and ionization structure of the outflow. The only assumed parameter is that the outflow has a full opening angle of 140° ($\Omega = 3.11\pi$ steradians). The peak $\dot{M}_o$ is 2.32 M$_\odot$ yr^{-1}. Note that the radius formally extends to infinity, and the last tick corresponds to the radius of x = 10.

angular covering fraction of the wind and v$_{cen}$ is the centroid velocity of the outflow (132 km s^{-1}). Previous studies assume a radius of 5 kpc, a full opening angle of 140° (and $\Omega = 3.11\pi$ steradians), solar metallicity, and no ionization correction (Rupke et al. 2005b; Martin 2005; Weiner et al. 2009; Rubin et al. 2014). Using the values from the Si IV line, and these assumptions, we derive a mass outflow rate for NGC 6090 of 7.32 M$_\odot$ yr^{-1}. However, previous studies typically use absorption lines of cooler gas like Na I, Mg II and Fe II (Rupke et al. 2005b; Martin 2005; Weiner et al. 2009; Martin & Bouché 2009; Rubin et al. 2014). If we use the Si II 1304 column density, a similar ionization potential to the previous outflow tracers, $\dot{M}_o$ rises to 22.6 M$_\odot$ yr^{-1}.

However, with our tightly constrained physical model of the outflow, now we only have to assume an angular covering fraction to calculate the mass outflow rate. Above, we derive a radius, a metallicity, and an ionization fraction for the outflows (see Table 5 for values). If we use the radius of peak optical depth (R$_p$ = 72.2 pc, at a w of 0.41), we calculate a total mass outflow rate of 0.81 M$_\odot$ yr^{-1}, 28 times lower than the $\dot{M}_o$ calculated using Si II.

While this calculation uses many of our derived values, it ignores the evolution of these quantities with velocity. In § 5.3 we find that the outflow is accelerated over short distances, in § 5.2 we find that the covering fraction decreases at large velocities, and in § 5.4 we find that the outflow is not a mass conserving flow, rather it evolves as x$^{-5.7}$. All of these impact how mass is distributed in velocity space. Using the scaling of the covering fraction, radius, and density with velocity, we define the mass outflow rate per velocity as

$$\begin{aligned}\dot{M}_o(r) &= \Omega C_f(r) v(r) \rho(r) r^2 \\ \dot{M}_o(w) &= \Omega C_f(R_i) v_\infty \mu m_p n_0 R_i^2 \frac{w}{(1-w^{1/\beta})^{2+\gamma+\alpha}} \\ &= 10.1\ M_\odot\ yr^{-1} \frac{w}{(1-w^{1/\beta})^{2+\gamma+\alpha}}\end{aligned} \quad (26)$$

where we use the values from Table 3 and Table 5 for the constants and the exponents, and the only assumed parameter is that Ω is 3.11π steradians. The $\dot{M}_o$ relation is not constant with velocity, as typically assumed (Figure 10): $\dot{M}_o$ increases rapidly at low velocities as the outflow accelerates, and declines at high velocities as the density and covering fraction of the outflow decline (Figure 8 and Figure 9).

At w of 0.35, the $\dot{M}_o$ relation peaks at a value of 2.3 M$_\odot$ yr^{-1}. This is a factor of ten times smaller than the Si II value calculated with previous assumptions for geometry, ionization fractions, and metallicities. Combining $\dot{M}_o$ with the derived outflow metallicity, we find that the maximum metal outflow rate is 0.07 M$_\odot$ yr^{-1}. This may constrain the impact of outflows on the mass-metallicity relationship (see above; Tremonti et al. 2004; Finlator & Davé 2008; Peeples & Shankar 2011; Andrews & Martini 2013; Zahid et al. 2014; Creasey et al. 2015; Christensen et al. 2015).

It is typical to normalize the mass outflow rate by the star formation rate to produce the "mass-loading" factor ($\eta = \dot{M}_o/SFR$; Rupke et al. 2005b). The global η is 0.09. This η is smaller than recent measurements from Heckman et al. (2015), who find an η near 0.3 for galaxies with SFRs near 30 M$_\odot$ yr^{-1}. However, Heckman et al. (2015) use the mean ISM metallicity of the sample (0.5 Z$_\odot$), do not calculate ionization fractions, and use a multiple of the half-light radius (typically 0.5-1 kpc) as the radius of the outflow. Other studies make similar assumptions about the metallicity and the ionization state, but assume constant outflow radii between 1-5 kpc (Rupke et al. 2005a; Martin et al. 2012; Rubin et al. 2014). These studies typically find η between 0.02 and 1 for SFRs and M_* similar to NGC 6090. The method outlined here does not rely on these uncertain assumptions and allows for these quantities to vary from galaxy to galaxy, reducing the scatter in the measurements.

The relatively small inner outflow radius implies that the local SFR may be more important than the global SFR. In Chisholm et al. (2015) we calculate the fraction of the total *GALEX* UV flux within the COS aperture to be 22%, leading to a SFR within the COS aperture of 5.55 M$_\odot$ yr^{-1}, however this does not account for the significant spatial variation in the IR flux and is only a crude approximation for the local SFR. Using this local SFR we calculate a local η within the COS aperture of 0.42.

The local and global η values are a factor of 5 and 22 times lower than the redshift independent η predicted by the FIRE simulation (Hopkins et al. 2012, 2014b; Muratov et al. 2015), although the high-mass FIRE galaxies at redshift 0 only have upper limits for η (Muratov et al. 2015). Hayward & Hopkins (2015) develop an analytical model that uses the momentum from stellar feedback to regulate star formation and drive outflows. A requirement of this model is that η depends on the gas fraction and the stellar mass of the host galaxy. Making approximations for these scalings with redshift, the analytical model predicts the mass-loading for a log(M_*/M$_\odot$) galaxy of 10.7 at $z \approx 0.03$ to be 0.05, in rough

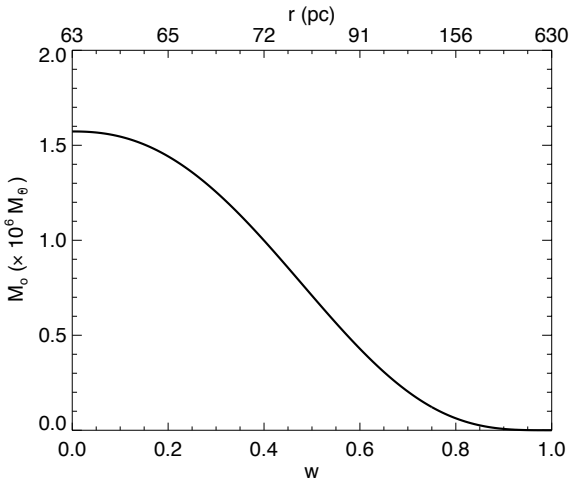

Figure 11. The total mass within the outflow at each velocity, as given by Equation 27. The total integrated outflow mass is 7.5×10^5 $M_\odot$.

agreement with the observed global η. While the outflow from NGC 6090 is weak compared to the SFR, Hayward & Hopkins (2015) predict that 10^9 $M_\odot$ galaxies drive outflows with an η of 10 at $z \sim 0$. In a future paper we will explore the scaling of $\dot{M}_o$ and η with host galaxy properties to better constrain these types of studies.

The total mass in the outflow (M_o) at a particular velocity is given by

$$M_o(w) = \Omega C_f(r) \mu m_p n_0 R_i^3 \left(\frac{1}{1-w^{1/\beta}}\right)^{3+\alpha+\gamma} = 1.5 \times 10^6 M_\odot \left(\frac{1}{1-w^{1/\beta}}\right)^{3+\alpha+\gamma} \quad (27)$$

This relation is shown in Figure 11. Like the density, the total mass in the Si IV outflow declines with velocity. The integrated mass between w of 0 and 1 is 7.5×10^5 $M_\odot$. While the current mass of outflowing gas is significantly lower than the measured H I mass of $10^{10.2}$ $M_\odot$ (van Driel et al. 2001), if $\dot{M}_o$ remains constant over the ~ 1 Gyr time scale of the merger, than the outflow will process (and enrich) 15% of the observed H I in NGC 6090, possibly leading to the metal enriched gas seen in the halos of galaxies (Tumlinson et al. 2011; Werk et al. 2014; Peeples et al. 2014; Wakker et al. 2015).

6 CONCLUSION

Here we measure a physically motivated mass outflow rate ($\dot{M}_o$) of the nearby starburst NGC 6090. To calculate $\dot{M}_o$, we first fit the optical depth with a Sobolev optical depth, and the covering fraction with a radial power-law (see Equation 12 and Figure 3). We then calculate the ionization corrections and the metallicity of the outflow using a Bayesian analysis, CLOUDY models, and the measured column densities (see Table 5 and Figure 4). The main results of this study are:

(i) The ionization model estimates the metallicity (1.61 $Z_\odot$), density (18.73 cm^{-3}) and the ionization parameter (log(U) = -1.85) of the outflow. The estimated H column density is consistent with that derived from the UV continuum extinction. The outflow is at least as metal enriched as the ISM of the host galaxy (see § 5.1).

(ii) Using the absorption line profile and ionization models, we determine that the inner edge (R_i) of the outflow is 63 pc from the starburst (see Equation 15), consistent with the absorption arising from the shredded blastwaves of supernovae remnants. Most of the outflow is constrained within 300 pc of the starburst (§ 5.1).

(iii) The covering fraction scales as $C_f = 1.0(r/R_i)^{-0.8\pm0.2}$ (Table 3). This scaling relation is consistent with predictions of clouds in pressure equilibrium with an adiabatically expanding external medium (§ 5.2). This warrents further study of whether outflowing clouds remain in pressure equilibrium with an external medium, and if a fractal cloud distribution could produce a similar scaling relation.

(iv) The Si IV outflow velocity scales with radius as $v = v_\infty(1 - R_i/r)^{0.43\pm0.07}$ (Figure 8 and Table 3), where v_∞ is the maximum velocity. We compare this velocity profile to models of different driving mechanisms, and find that an r^{-2} force law matches the observed profile (see Figure 8 and § 5.3).

(v) The outflow density decreases with radius as $n \propto r^{-5.7\pm1.5}$ (Figure 9), which declines more rapidly than a mass conserving flow (§ 5.4). This rapid density reduction could be due to interactions between the outflowing clouds and a hotter wind.

(vi) Combining all of our measurements, we derive a maximum mass outflow rate ($\dot{M}_o$) of 2.3 $M_\odot$ yr^{-1} (see Figure 10). The mass-loading factor (mass outflow rate divided by star formation rate) is 0.09. The $\dot{M}_o$ is a factor of 10 lower than the $\dot{M}_o$ calculated using common assumptions for ionization state, metallicity, and geometry (see § 5.5).

In future work, we will continue this analysis for a larger sample of star forming galaxies, studying how the outflow properties (metallicity, initial radius, mass outflow rate) scale with host galaxy properties. These scaling relations will constrain future models of galaxy evolution.

ACKNOWLEDGMENTS

We thank the anonymous referee for constructive comments that strengthened the paper. Joseph Cassinelli inspired this work with helpful conversations and notes. We thank Bart Wakker for help with the data reduction and discussions on the analysis.

Support for program 13239 was provided by NASA through a grant from the Space Telescope Science Institute, which is operated by the Association of Universities for Research in Astronomy, Inc., under NASA contract NAS 5-26555. Some of the data presented in this paper were obtained from the Mikulski Archive for Space Telescopes (MAST). STScI is operated by the Association of Universities for Research in Astronomy, Inc., under NASA contract NAS 5-26555.

All of the HST data presented in this paper were obtained from the Mikulski Archive for Space Telescopes

(MAST). STScI is operated by the Association of Universities for Research in Astronomy, Inc., under NASA contract NAS5-26555. Support for MAST for non-HST data is provided by the NASA Office of Space Science via grant NNX09AF08G and by other grants and contracts.

Funding for the Sloan Digital Sky Survey (SDSS) has been provided by the Alfred P. Sloan Foundation, the Participating Institutions, the National Aeronautics and Space Administration, the National Science Foundation, the U.S. Department of Energy, the Japanese Monbukagakusho, and the Max Planck Society. The SDSS Web site is http: www.sdss.org/. The SDSS is managed by the Astrophysical Research Consortium (ARC) for the Participating Institutions. The Participating Institutions are The University of Chicago, Fermilab, the Institute for Advanced Study, the Japan Participation Group, The Johns Hopkins University, Los Alamos National Laboratory, the Max-Planck-Institute for Astronomy (MPIA), the Max-Planck-Institute for Astrophysics (MPA), New Mexico State University, University of Pittsburgh, Princeton University, the United States Naval Observatory, and the University of Washington.

REFERENCES

Abazajian K. N., et al., 2009, ApJS, 182, 543
Adelberger K. L., Steidel C. C., Shapley A. E., Pettini M., 2003, ApJ, 584, 45
Andrews B. H., Martini P., 2013, ApJ, 765, 140
Arribas S., Colina L., Bellocchi E., Maiolino R., Villar-Martín M., 2014, A&A, 568, A14
Baldwin J. A., Ferland G. J., Martin P. G., Corbin M. R., Cota S. A., Peterson B. M., Slettebak A., 1991, ApJ, 374, 580
Bland J., Tully B., 1988, Nature, 334, 43
Brinchmann J., Charlot S., White S. D. M., Tremonti C., Kauffmann G., Heckman T., Brinkmann J., 2004, MNRAS, 351, 1151
Brüggen M., Scannapieco E., 2016, preprint, (arXiv:1602.01843)
Bustard C., Zweibel E. G., D'Onghia E., 2016, ApJ, 819, 29
Calzetti D., Armus L., Bohlin R. C., Kinney A. L., Koornneef J., Storchi-Bergmann T., 2000, ApJ, 533, 682
Chen Y.-M., Tremonti C. A., Heckman T. M., Kauffmann G., Weiner B. J., Brinchmann J., Wang J., 2010, AJ, 140, 445
Chevalier R. A., Clegg A. W., 1985, Nature, 317, 44
Chisholm J., Tremonti C. A., Leitherer C., Chen Y., Wofford A., Lundgren B., 2015, ApJ, 811, 149
Chisholm J., Tremonti C. A., Leitherer C., Chen Y., Wofford A., 2016, MNRAS, 457, 3133
Christensen C. R., Davé R., Governato F., Pontzen A., Brooks A., Munshi F., Quinn T., Wadsley J., 2015, preprint, (arXiv:1508.00007)
Cooper J. L., Bicknell G. V., Sutherland R. S., Bland-Hawthorn J., 2008, ApJ, 674, 157
Creasey P., Theuns T., Bower R. G., 2015, MNRAS, 446, 2125
Denicoló G., Terlevich R., Terlevich E., 2002, MNRAS, 330, 69
Diamond-Stanic A. M., Moustakas J., Tremonti C. A., Coil A. L., Hickox R. C., Robaina A. R., Rudnick G. H., Sell P. H., 2012, ApJ, 755, L26
Draine B. T., 2011, Physics of the Interstellar and Intergalactic Medium
Erb D. K., 2015, Nature, 523, 169
Erb D. K., Quider A. M., Henry A. L., Martin C. L., 2012, ApJ, 759, 26
Everett J. E., Zweibel E. G., Benjamin R. A., McCammon D., Rocks L., Gallagher III J. S., 2008, ApJ, 674, 258
Feigelson E. D., Jogesh Babu G., 2012, Modern Statistical Methods for Astronomy
Ferland G. J., et al., 2013, rmxaa, 49, 137
Finlator K., Davé R., 2008, MNRAS, 385, 2181
France K., Beasley M., Keeney B. A., Danforth C. W., Froning C. S., Green J. C., Shull J. M., 2009, ApJ, 707, L27
Fujita A., Martin C. L., Mac Low M.-M., New K. C. B., Weaver R., 2009, ApJ, 698, 693
Gil de Paz A., Madore B. F., Pevunova O., 2003, ApJS, 147, 29
Green J. C., et al., 2012, ApJ, 744, 60
Griffiths R. E., Ptak A., Feigelson E. D., Garmire G., Townsley L., Brandt W. N., Sambruna R., Bregman J. N., 2000, Science, 290, 1325
Grimes J. P., et al., 2009, ApJS, 181, 272
Hamann F., Barlow T. A., Junkkarinen V., Burbidge E. M., 1997, ApJ, 478, 80
Hayward C. C., Hopkins P. F., 2015, preprint, (arXiv:1510.05650)
Heckman T. M., Armus L., Miley G. K., 1990, ApJS, 74, 833
Heckman T. M., Lehnert M. D., Strickland D. K., Armus L., 2000, ApJS, 129, 493
Heckman T. M., et al., 2011, ApJ, 730, 5
Heckman T. M., Alexandroff R. M., Borthakur S., Overzier R., Leitherer C., 2015, ApJ, 809, 147
Hopkins P. F., Quataert E., Murray N., 2012, MNRAS, 421, 3522
Hopkins P. F., Kereš D., Oñorbe J., Faucher-Giguère C.-A., Quataert E., Murray N., Bullock J. S., 2014a, MNRAS, 445, 581
Hopkins P. F., Kereš D., Oñorbe J., Faucher-Giguère C.-A., Quataert E., Murray N., Bullock J. S., 2014b, MNRAS, 445, 581
Indriolo N., Geballe T. R., Oka T., McCall B. J., 2007, ApJ, 671, 1736
Jarosik N., et al., 2011, ApJS, 192, 14
Kauffmann G., et al., 2003, MNRAS, 341, 33
Kewley L. J., Groves B., Kauffmann G., Heckman T., 2006, MNRAS, 372, 961
Kim C.-G., Ostriker E. C., 2015, ApJ, 802, 99
Kimm T., Cen R., Devriendt J., Dubois Y., Slyz A., 2015, MNRAS, 451, 2900
Klein R. I., McKee C. F., Colella P., 1994, ApJ, 420, 213
Kornei K. A., Shapley A. E., Martin C. L., Coil A. L., Lotz J. M., Schiminovich D., Bundy K., Noeske K. G., 2012, ApJ, 758, 135
Lamers H. J. G. L. M., Cassinelli J. P., 1999, Introduction to Stellar Winds
Leitherer C., et al., 1999, ApJS, 123, 3
Leitherer C., Li I.-H., Calzetti D., Heckman T. M., 2002, ApJS, 140, 303
Leitherer C., Ortiz Otálvaro P. A., Bresolin F., Kudritzki R.-P., Lo Faro B., Pauldrach A. W. A., Pettini M., Rix S. A., 2010, ApJS, 189, 309
Leitherer C., Chandar R., Tremonti C. A., Wofford A., Schaerer D., 2013, ApJ, 772, 120
Leroy A. K., et al., 2015, ApJ, 814, 83
Lynds C. R., Sandage A. R., 1963, ApJ, 137, 1005
Mac Low M.-M., McCray R., Norman M. L., 1989, ApJ, 337, 141
Markwardt C. B., 2009, in Bohlender D. A., Durand D., Dowler P., eds, Astronomical Society of the Pacific Conference Series Vol. 411, Astronomical Data Analysis Software and Systems XVIII. p. 251 (arXiv:0902.2850)
Martin C. L., 2005, ApJ, 621, 227
Martin C. L., Bouché N., 2009, ApJ, 703, 1394
Martin C. L., Shapley A. E., Coil A. L., Kornei K. A., Bundy K., Weiner B. J., Noeske K. G., Schiminovich D., 2012, ApJ, 760, 127
Matsushita S., Kawabe R., Matsumoto H., Tsuru T. G., Kohno K., Morita K.-I., Okumura S. K., Vila-Vilaró B., 2000, ApJ,

545, L107
McKee C. F., Ostriker J. P., 1977, ApJ, 218, 148
Meynet G., Maeder A., Schaller G., Schaerer D., Charbonnel C., 1994, A&AS, 103, 97
Muratov A. L., Kereš D., Faucher-Giguère C.-A., Hopkins P. F., Quataert E., Murray N., 2015, MNRAS, 454, 2691
Murray N., Quataert E., Thompson T. A., 2005, ApJ, 618, 569
Murray N., Martin C. L., Quataert E., Thompson T. A., 2007, ApJ, 660, 211
Murray N., Ménard B., Thompson T. A., 2011, ApJ, 735, 66
Newman S. F., et al., 2012, ApJ, 761, 43
Osterbrock D. E., Tran H. D., Veilleux S., 1992, ApJ, 389, 305
Östlin G., Hayes M., Kunth D., Mas-Hesse J. M., Leitherer C., Petrosian A., Atek H., 2009, AJ, 138, 923
Ostriker J. P., McKee C. F., 1988, Rev. Mod. Phys., 60, 1
Peeples M. S., Shankar F., 2011, MNRAS, 417, 2962
Peeples M. S., Werk J. K., Tumlinson J., Oppenheimer B. D., Prochaska J. X., Katz N., Weinberg D. H., 2014, ApJ, 786, 54
Pettini M., Steidel C. C., Adelberger K. L., Dickinson M., Giavalisco M., 2000, ApJ, 528, 96
Pettini M., Rix S. A., Steidel C. C., Adelberger K. L., Hunt M. P., Shapley A. E., 2002, ApJ, 569, 742
Prochaska J. X., Kasen D., Rubin K., 2011, ApJ, 734, 24
Rubin R. H., Dufour R. J., Walter D. K., 1993, ApJ, 413, 242
Rubin K. H. R., Prochaska J. X., Ménard B., Murray N., Kasen D., Koo D. C., Phillips A. C., 2011, ApJ, 728, 55
Rubin K. H. R., Prochaska J. X., Koo D. C., Phillips A. C., Martin C. L., Winstrom L. O., 2014, ApJ, 794, 156
Rupke D. S., Veilleux S., Sanders D. B., 2005a, ApJS, 160, 87
Rupke D. S., Veilleux S., Sanders D. B., 2005b, ApJS, 160, 115
Sakamoto K., Aalto S., Combes F., Evans A., Peck A., 2014, ApJ, 797, 90
Savage B. D., Sembach K. R., 1991, ApJ, 379, 245
Scannapieco E., Brüggen M., 2015, ApJ, 805, 158
Scarlata C., Panagia N., 2015, ApJ, 801, 43
Schlegel D. J., Finkbeiner D. P., Davis M., 1998, ApJ, 500, 525
Sedov L. I., 1959, Similarity and Dimensional Methods in Mechanics
Shapiro P. R., Field G. B., 1976, ApJ, 205, 762
Shapley A. E., Steidel C. C., Pettini M., Adelberger K. L., 2003, ApJ, 588, 65
Shopbell P. L., Bland-Hawthorn J., 1998, ApJ, 493, 129
Sobolev V. V., 1960, Moving envelopes of stars
Socrates A., Davis S. W., Ramirez-Ruiz E., 2008, ApJ, 687, 202
Songaila A., 1997, ApJ, 490, L1
Steidel C. C., Erb D. K., Shapley A. E., Pettini M., Reddy N., Bogosavljević M., Rudie G. C., Rakic O., 2010, ApJ, 717, 289
Storchi-Bergmann T., Calzetti D., Kinney A. L., 1994, ApJ, 429, 572
Strickland D. K., Heckman T. M., 2009, ApJ, 697, 2030
Strickland D. K., Stevens I. R., 2000, MNRAS, 314, 511
Strickland D. K., Heckman T. M., Colbert E. J. M., Hoopes C. G., Weaver K. A., 2004, ApJ, 606, 829
Taylor G., 1950, Royal Society of London Proceedings Series A, 201, 159
Thompson T. A., Quataert E., Murray N., 2005, ApJ, 630, 167
Thompson T. A., Quataert E., Zhang D., Weinberg D. H., 2016, MNRAS, 455, 1830
Tremonti C. A., et al., 2004, ApJ, 613, 898
Tumlinson J., et al., 2011, Science, 334, 948
Veilleux S., Shopbell P. L., Rupke D. S., Bland-Hawthorn J., Cecil G., 2003, AJ, 126, 2185
Veilleux S., Cecil G., Bland-Hawthorn J., 2005, ARA&A, 43, 769
Verhamme A., Schaerer D., Maselli A., 2006, A&A, 460, 397
Wakker B. P., Hernandez A. K., French D. M., Kim T.-S., Oppenheimer B. D., Savage B. D., 2015, ApJ, 814, 40
Weaver R., McCray R., Castor J., Shapiro P., Moore R., 1977, ApJ, 218, 377
Weiner B. J., et al., 2009, ApJ, 692, 187
Weiß A., Walter F., Neininger N., Klein U., 1999, A&A, 345, L23
Werk J. K., et al., 2014, ApJ, 792, 8
Westmoquette M. S., Smith L. J., Gallagher III J. S., Trancho G., Bastian N., Konstantopoulos I. S., 2009, ApJ, 696, 192
Wood C. M., Tremonti C. A., Calzetti D., Leitherer C., Chisholm J., Gallagher J. S., 2015, MNRAS, 452, 2712
Zahid H. J., Dima G. I., Kudritzki R.-P., Kewley L. J., Geller M. J., Hwang H. S., Silverman J. D., Kashino D., 2014, ApJ, 791, 130
Zhang D., Thompson T. A., Quataert E., Murray N., 2015, preprint, (arXiv:1507.01951)
Zhu G. B., et al., 2015, ApJ, 815, 48
de Blok W. J. G., Fraternali F., Heald G. H., Adams E. A. K., Bosma A., Koribalski B. S., the HI Science Working Group 2015, preprint, (arXiv:1501.01211)
de Vaucouleurs G., de Vaucouleurs A., Corwin Jr. H. G., Buta R. J., Paturel G., Fouqué P., 1991, Third Reference Catalogue of Bright Galaxies. Volume I: Explanations and references. Volume II: Data for galaxies between 0^h and 12^h. Volume III: Data for galaxies between 12^h and 24^h.
van Driel W., Gao Y., Monnier-Ragaigne D., 2001, A&A, 368, 64

This paper has been typeset from a TEX/LATEX file prepared by the author.